The Astrophysical Journal, 1011:133 (22pp), 2026 November 1 https://doi.org/10.3847/1538-4357/aea4b2
© 2026. The Author(s). Published by the American Astronomical Society.
OPEN ACCESS

Sinking Silicates. I. Characterizing the Benchmark System Containing the T0 Brown Dwarf CWISEJ210640.16+250729.0 using JWST

Austin Rothermich[1,2,3,4], Jacqueline K. Faherty[1,4], Ben Burningham[5], Catherine Manea[6], Emily Calamari[1], Genaro Suárez[1], Daniella C. Bardalez Gagliuffi[7], John M. Brewer[8], Kelle L. Cruz[1,9,10], Josefine Gaarn[5], Jonathan Gagné[11,12], Eileen C. Gonzales[8], Marina E. Gemma[1,13,14], Viktória Kecskeméthy[5], Mark S. Marley[15], Caprice L. Phillips[16,20], Channon Visscher[17,18], Johanna M. Vos[19], and Niall Whiteford[1]
[1] Department of Astrophysics, American Museum of Natural History, New York, NY, USA
[2] Department of Physics, Graduate Center, City University of New York, 365 5th Avenue, New York, NY 10016, USA
[3] Department of Physics and Astronomy, Hunter College, City University of New York, 695 Park Avenue, New York, NY, 10065, USA
[4] Backyard Worlds: Planet 9, USA
[5] Department of Physics, Astronomy and Mathematics, University of Hertfordshire, Hatfield, UK
[6] Department of Physics & Astronomy, University of Utah, Salt Lake City, UT 84112, USA
[7] Department of Physics & Astronomy, Amherst College, Amherst, MA, USA
[8] Department of Physics & Astronomy, San Francisco State University, 1600 Holloway Avenue, San Francisco, CA 94132, USA
[9] Department of Physics and Astronomy, Hunter College, City University of New York, New York, NY, USA
[10] Department of Physics, Graduate Center, City University of New York, New York, NY, USA
[11] Planétarium Rio Tinto Alcan, Montreal, Quebec, Canada
[12] Département de Physique, Université de Montréal, Montreal, Quebec, Canada
[13] Department of Geosciences, Stony Brook University, Stony Brook, NY 11794, USA
[14] Department of Earth and Planetary Sciences, American Museum of Natural History, New York, NY 10024, USA
[15] Lunar and Planetary Laboratory, University of Arizona, 1629 E. University Boulevard, Tucson, AZ 85721, USA
[16] Department of Astronomy & Astrophysics, University of California, Santa Cruz, CA 95064, USA
[17] Department of Chemistry and Planetary Sciences, Dordt University, Sioux Center, IA, USA
[18] Center for Exoplanetary Systems, Space Science Institute, Boulder, CO, USA
[19] School of Physics, Trinity College Dublin, The University of Dublin, Dublin, Ireland
Received 2025 October 24; revised 2026 September 2; accepted 2026 September 7; published 2026 October 29

Abstract

In this study, we present the full (97.3% complete) 0.8–12.5 μm spectral energy distribution (SED) of an L/T transition object, CWISE J210640.16+250729.0 (CW 2106), using the James Webb Space Telescope (JWST). We provide a full characterization of the host star's elemental abundances and age. We empirically derive the bolometric luminosity (≈ -4.825 dex) of CW 2106, and obtain estimates of its mass ($M \approx 50$–$62\ M_{\rm Jup}$), radius ($R \approx 0.83$–$0.87\ R_{\rm Jup}$), effective temperature ($T_{\rm eff} \approx 1213$ K), and surface gravity ($\log g \approx 5.28$ dex). We find the near-infrared (near-IR) spectrum (0.8–2.5 μm) is best reproduced with cloudy atmospheric models while the mid-infrared (mid-IR) spectrum (5–12.5 μm) is best reproduced with cloudless models. This suggests a cloud layer restricted to only the deepest observable parts of the atmosphere and is qualified by the lack of a 9 μm silicate feature. Making use of the Mg/Si ratio of the primary, alongside thermochemical models, we predict the clouds in CW 2106 to be composed primarily of enstatite ($MgSiO_3$), removing $\sim$23% of the bulk oxygen out of the atmosphere. Future retrieval studies will be able to help investigate the existence and full impact of these cloud species.

Unified Astronomy Thesaurus concepts: Brown dwarfs (185); T dwarfs (1679); Stellar atmospheres (1584); Stellar abundances (1577); Spectral energy distribution (2129)

1. Introduction

Brown dwarfs, objects with masses below the hydrogen burning mass limit (HBML) ($\sim$78.5 $M_{\rm Jup}$; G. Chabrier et al. 2023), represent the lowest mass products of the stellar initial mass function (IMF; J. D. Kirkpatrick et al. 2021; W. M. J. Best et al. 2024; J. D. Kirkpatrick et al. 2024). While brown dwarfs may form in a similar process as stars (M. R. Bate et al. 2002), the lack of hydrogen fusion in their cores results in a drastically different evolution than for objects whose masses are above the HBML. Unlike stars on the main sequence, which remain relatively stable over long periods of time, brown dwarfs slowly cool and contract as they age. As a consequence, the continually cooling atmospheres of brown dwarfs give rise to different molecular species and condensates as they age, morphing them from the warm "L" spectral types into the cooler T-types, and eventually to the cold Y spectral class (A. Burrows et al. 1997; J. D. Kirkpatrick 2005; M. C. Cushing et al. 2011).

A particularly interesting stage of brown dwarf evolution occurs during the phase in which they cool below L-dwarf temperatures into that of the T-dwarfs, the aptly named L/T transition. This transition, which occurs over a narrow temperature range ($T_{\rm eff} \approx$ 1400–1100 K; J. D. Kirkpatrick et al. 2000; M. C. Cushing et al. 2008; D. C. Stephens et al. 2009), results in distinct observed differences in spectral morphology. Prominent methane (CH_4) bands appear in the J, H, and K bands as CH_4 replaces carbon monoxide (CO) as

[20] NASA Sagan Fellow.

Original content from this work may be used under the terms of the Creative Commons Attribution 4.0 licence. Any further distribution of this work must maintain attribution to the author(s) and the title of the work, journal citation and DOI.

the main carbon bearing molecule (A. J. Burgasser et al. 2002b). Silicate condensates (i.e., clouds), such as enstatite ($MgSiO_3$) and forsterite (Mg_2SiO_4), which form in the upper atmospheres of the warmer L-dwarfs (K. Lodders & B. Fegley 2006) sediment below the photosphere during this transition (G. Suárez & S. Metchev 2022). Due in part to the difficulty in cloud modeling, no current self-consistent atmospheric or evolutionary models can fully and accurately reproduce the L/T transition (see C. V. Morley et al. 2024 for more discussion).

Obtaining precise fundamental parameters of L/T transition objects, such as mass (M), radius (R), effective temperature ($T_{\rm eff}$), and bolometric luminosity ($L_{\rm bol}$), is a crucial step in understanding this stage of brown dwarf evolution. Young (i.e., low surface gravity) brown dwarfs along the L/T transition, for example, appear to have cooler $T_{\rm eff}$'s and redder colors than their field-aged counterparts (e.g., S. A. Metchev & L. A. Hillenbrand 2006; K. L. Luhman 2007). Cloud sedimentation at the L/T boundary has been found to be less efficient in the younger objects as well (e.g., M. S. Marley et al. 2012; G. Suárez & S. Metchev 2023). The canonical approach to deriving these fundamental parameters is through the assemblage of broad wavelength coverage spectral energy distributions (SEDs) using flux calibrated optical to infrared spectrophotometry along with evolutionary models (see D. C. Stephens et al. 2009; J. C. Filippazzo et al. 2015; A. Sanghi et al. 2023). This method relies on having precise distances and ages, the main sources of error in the derivation of fundamental parameters.

While parallaxes for brown dwarfs are becoming more common, with ∼361 objects $\lesssim$25 pc having a trigonometric parallax (T. J. Dupuy & M. C. Liu 2012; J. K. Faherty et al. 2012; D. C. Bardalez Gagliuffi et al. 2019; W. M. J. Best et al. 2020; Gaia Collaboration et al. 2021; J. D. Kirkpatrick et al. 2021), ages for brown dwarfs are still difficult to obtain. The majority of brown dwarf ages come from objects belonging to young moving groups (e.g., M. C. Liu et al. 2013; J. Gagné et al. 2014, 2015; J. K. Faherty et al. 2016) and are therefore limited to ages $\lesssim$1 Gyr. For isolated field brown dwarfs, which comprise the majority of the known brown dwarfs, there are no observational methods that can precisely constrain their ages. Instead, the field population requires the use of age estimates with extremely large error bars. This means for a typical brown dwarf, whose age is poorly constrained, estimates for mass, radius, $T_{\rm eff}$, and log g obtained from evolutionary models are strongly impacted by the choice of age distribution.

To illuminate this, we can take a look at the analyses performed by J. C. Filippazzo et al. (2015) and A. Sanghi et al. (2023), whose fundamental parameter samples contain 130 overlapping objects. The two studies made use of different age distributions for field objects: J. C. Filippazzo et al. (2015) used a uniform distribution spanning 0.5–10 Gyr, while A. Sanghi et al. (2023) implemented the age distribution from T. J. Dupuy & M. C. Liu (2017), a probability density function spanning 0.01–10 Gyr, which prefers younger ages, leading to different fundamental parameters for ∼37 objects. 2MASS J03185403-3421292 (a field age L7; J. D. Kirkpatrick et al. 2008), for example, has differences in mass, radius, $T_{\rm eff}$, and log g of ∼82%, 36%, 18%, and 19%, respectively. Many of the 37 objects with differences between the two studies are likewise field objects, whose parameters are similarly impacted by the change in age distribution choice.

Benchmark brown dwarfs—defined here-in as objects that are comoving with a higher mass star—are an ideal sample for deriving fundamental parameters (e.g., A. Rothermich et al. 2024). The coevality of the pair means that many of the parameters derived for the host star, such as distance, age, and metallicity, are also applicable for its brown dwarf companion. Host star parallaxes are widely available thanks to all-sky astrometry programs such as Gaia (Gaia Collaboration et al. 2016), providing distances for their brown dwarf companions without the need for observationally expensive parallax programs. Many host stars are also ideal for age dating, either through comparisons with stellar isochrone models (e.g., J. Choi et al. 2016), white dwarf cooling models (e.g., M. A. Wood 1995; G. Fontaine et al. 2001; I. Renedo et al. 2010; R. Kiman et al. 2022), or gyrochronology (e.g., A. Skumanich 1972; E. E. Mamajek & L. A. Hillenbrand 2008; M. Popinchalk et al. 2021), all of which make it possible to derive well constrained ages >1 Gyr, something not currently possible for isolated brown dwarfs. The fundamental parameters derived for these benchmarks are therefore free from the errors associated with probabilistic age distribution estimates, resulting in more precise estimates of mass, radius, $T_{\rm eff}$, and log g than otherwise possible for typical field objects.

Studying benchmark systems provides another advantage over isolated field objects in that the elemental abundances of the system can be constrained through the host star, particularly if it is a solar-like F-, G-, or K-type star for which these analyses are best suited. Assuming the two objects formed out of the same natal environment, presumably the pair will share the same primordial makeup. Indeed, studies comparing the abundances between stellar binary twins, pairs in which $\Delta T_{\rm eff} < 200$K, have found that ∼80% of wide systems (300–50,000 au) share a similar chemical makeup within ∼0.02 dex (K. Hawkins et al. 2020; J. K. Teske 2024). This trend appears to hold even in the widest pairs, with ∼70% of wide comoving stellar twins ($\lesssim$100,000 au) being chemically homogeneous (e.g., T. Nelson et al. 2021; D. Yong et al. 2023). Brown dwarf benchmark systems share a common formation pathway with typical stellar binaries (e.g., M. R. Bate 2009, 2012), and as such are also expected to be chemically similar to their stellar relative.

Newer approaches such as spectral inversion techniques, otherwise known as retrievals, are now able to model a brown dwarf's atmospheric gas abundances, $T_{\rm eff}$, cloud properties, and other fundamental parameters (M. R. Line et al. 2015; E. C. Gonzales et al. 2020; B. Burningham et al. 2021; J. A. Zalesky et al. 2022; J. M. Vos et al. 2023; H. Kothari et al. 2024; B. W. P. Lew et al. 2024). However, properties such as atmospheric gas abundances are still difficult to model, relying on sometimes incomplete or incorrect absorption cross sections (B. Burningham et al. 2017). Benchmark brown dwarfs, with elemental abundances known a priori, which can be used to ground the analysis, consequently represent ideal targets for retrieval studies. While retrievals are able to estimate the atmospheric abundances of a brown dwarf, the abundances provided for benchmark systems via their host stars represent the bulk composition. These bulk abundances can be used, for example, along with retrieved abundances to investigate oxygen sequestration due to cloud condensates (see E. Calamari et al. 2022; J. Wang et al. 2022;

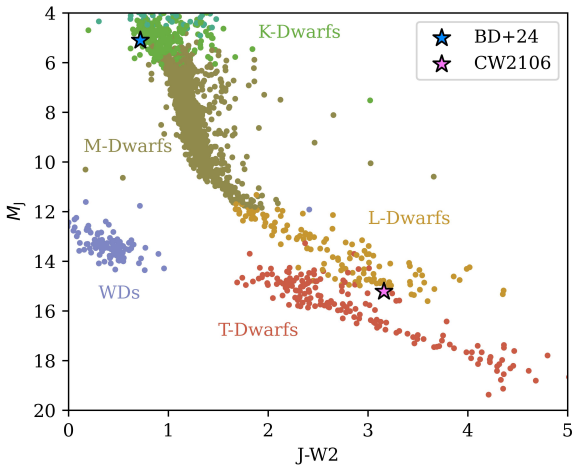


Figure 1. Color–magnitude diagram for the 20 pc parallax sample of J. D. Kirkpatrick et al. (2024), with the different spectral types colored and labeled. BD+24 is shown as the blue pointed star, with CW 2106 shown as a pink pointed star.

J. Gaarn et al. 2023), or to predict the cloud species expected to form (E. Calamari et al. 2024; C. L. Phillips et al. 2024).

In this paper, we present the first SED and fundamental parameters of CWISE J210640.16+250729.0, an L-T transition companion to a K-dwarf. In Section 2, we present an overview of the discovery and properties of the system. Section 3 describes the observations and data reduction carried out for both the brown dwarf and its host star. We characterize the host star in Section 4, including an analysis of its elemental abundances and age determination. In Section 5, we assign a spectral type to CWISE J210640.16+250729.0 and derive its fundamental parameters using its full SED. Section 6 presents a deeper look into the spectral features observed in the SED of CWISE J210640.16+250729.0, while Section 7 compares its SED with forward model grids. In Section 8, we discuss the expected species of silicate clouds using recent thermochemical models. The results of the forward model comparisons are placed into context with the system's known properties in Section 9. Our conclusions are presented in Section 10.

2. System Overview

CWISE J210640.16+250729.0 (hereafter referred to as CW 2106) was found to be a comoving companion to the K6V dwarf BD+24 4329 (BD+24 from this point on) in A. Rothermich et al. (2024). After initially identifying the pair visually through the citizen science project Backyard Worlds: Planet 9 (M. J. Kuchner et al. 2017), A. Rothermich et al. (2024) used the Bayesian algorithm `CoMover` (J. Gagné et al. 2021) to assess the likelihood of the pair being physically associated using each object's coordinates, proper motions, and parallax (for CW 2106, its photometric distance estimate), and their associated errors. They found the system had a 99.4% probability of being associated, above the 90% cutoff used to determine "high likelihood" systems. The pair have an angular separation of 1124″ (∼18.′7), translating to a projected physical separation of ∼38,000 au. While no spectrum of CW 2106 was presented, CW 2106 was assigned an estimated phototype of ∼T2.

On a Gaia color–magnitude diagram (CMD), BD+24 has a normal brightness compared to objects of a similar color. However, it stands out a bit more when using infrared colors as shown in the CMD in Figure 1, with BD+24 being slightly underluminous in J for its $J - W2$ color. In contrast, CW 2106 appears to be underluminous for its $J - W2$ color in Figure 1. CW 2106 was estimated to have a mass of ∼36 $M_{\rm Jup}$ (A. Rothermich et al. 2024), giving the system a mass ratio of 0.05, a binding energy of $E_B = 0.1 \times 10^{41}$ erg, and a dynamical dissipation lifetime of 4 Gyr. Summaries of the BD +24 and CW 2106 system properties are provided in Table 1.

3. Observations

In this section, we present new data for the CW 2106 system. All data is available from the SIMPLE Archive.[21]

3.1. Magellan/FIRE

CW 2106 was observed with the Folded-port Infrared Echellette (FIRE; R. A. Simcoe et al. 2013) on the Magellan Baade telescope, located at the Las Campanas Observatory. Near infrared data (0.82–2.51 μm) was taken on 2024 May 28 with the instrument in echelle mode, providing a moderate resolving power of $\lambda/\Delta\lambda \approx 6000$. Light cirrus was present throughout the observations, with seeing between ∼0.″7–1.″0 and at an airmass of 1.79. The telluric star HIP 92177 was observed at an airmass of 2.08 after the science observation. Data were reduced using the FIREHOSE package, which is based on the MASE and SpeX reduction tools (W. D. Vacca et al. 2003; M. C. Cushing et al. 2004; J. J. Bochanski et al. 2009). The final FIRE spectrum is shown in Figure 2.

3.2. JWST

3.2.1. Data Acquisition

CW 2106 was observed with The James Webb Space Telescope (JWST; J. Rigby et al. 2023) on 2024 June 24 as part of the cycle 2 GO program 3670 (PI: Burningham). Observations were performed with the Near-Infrared Spectrograph (NIRSpec; P. Jakobsen et al. 2022) and Mid-Infrared Instrument (MIRI; G. H. Rieke et al. 2015).

NIRSpec was used in low-resolution prism mode with the S200A1 fixed slit to obtain near infrared data (0.6–5.3 μm) with a resolving power of $\lambda/\Delta\lambda \approx 100$. Target acquisition was carried out using the WATA method, clear filter, subarray 32 and NRSRAPID readout pattern. The science observation was performed with 10 groups per integration, 1 integration per exposure, and 3 dithers for a total integration time of 51.475 s. The resulting spectrum has an average signal-to-noise (SNR) of ∼52.

MIRI was used to obtain mid-infrared data (5–14 μm) low-resolution spectrometer (LRS) in fixed-slit mode providing a resolving power of $\lambda/\Delta\lambda \approx 100$ at 7.5 μm. Target acquisition was completed using the F1000W filter and FAST readout pattern. Science observations were taken with the FASTR1 readout pattern, 100 groups/integration, 1 integration/exposure, and 2 dithers resulting in a total exposure time of 555.008 s, resulting in an average SNR of ∼72 across the full wavelength coverage.

[21] https://simple-bd-archive.org/load_solo/CWISE%20J210640.16+250729.0

Table 1
BD+24 4329 and CW 2106 System Properties

Property	BD+24 4329	Reference	CW 2106	Reference
SpType	K6V	Steph1986	T0 ± 1	This Work
R.A. (deg)	317.00781	DR3	316.66735	CW 2020
Decl. (deg)	25.17551	DR3	25.12471	CW 2020
PMRA (mas yr^{-1})	−21.89 ± 0.01	DR3	−39.5 ± 14.7	CW 2020
PMDec (mas yr^{-1})	−162.53 ± 0.01	DR3	−132.6 ± 13.3	CW 2020
RV (km s^{-1})	−5.31 ± 0.15	DR3	⋯	⋯
$V\sin(i)$ (km s^{-1})	6.02 ± 2.19	DR3	⋯	⋯
Plx (mas)	29.31 ± 0.01	DR3	⋯	⋯
		Photometry		
g_{PS1} (mag)	10.21 ± 0.04	PS1	⋯	⋯
r_{PS1} (mag)	10.11 ± 0.01	PS1	⋯	⋯
i_{PS1} (mag)	9.53 ± 0.15	PS1	⋯	⋯
z_{PS1} (mag)	10.08 ± 0.01	PS1	21.19 ± 0.08	PS1
y_{PS1} (mag)	9.97 ± 0.09	PS1	19.85 ± 0.16	PS1
J (mag)	7.77 ± 0.02	2MASS	17.88 ± 0.05	UHS
H (mag)	7.19 ± 0.03	2MASS	⋯	⋯
K (mag)	7.06 ± 0.03	2MASS	⋯	⋯
W1 (mag)	6.92 ± 0.01	CW 2020	15.33 ± 0.02	CW 2020
W2 (mag)	7.05 ± 0.01	CW 2020	14.72 ± 0.02	CW 2020
W3 (mag)	7.04 ± 0.02	AllWISE	12.56[b]	CW 2020
W4 (mag)	7.07 ± 0.10	AllWISE	8.83[b]	CW 2020
		Fundamental Parameters		
(dex)	−0.729 ± 0.039	Tuch2024	−4.825 ± 0.005	This Work
$T_{\rm eff}$ (K)	4511 ± 21	This Work	1213 ± 21	This Work
Mass ($M_\odot$, $M_{\rm Jup}$)	0.71 ± 0.04	Tuch2024	56 ± 6	This Work
Radius ($R_\odot$, $R_{\rm Jup}$)	0.71 ± 0.04	Tuch2024	0.85 ± 0.02	This Work
log g (dex)	4.42 ± 0.05	This Work	5.28 ± 0.07	This Work
Age (Gyr)	$3.3^{+0.7}_{-0.5}$	This Work	⋯	⋯

Notes.
[a] The probability of the pair being physically associated.
[b] Denotes magnitude limit.
References. DR3, Gaia Collaboration et al. (2023); CW 2020, F. Marocco et al. (2021); 2MASS, M. F. Skrutskie et al. (2006); PS1, K. C. Chambers et al. (2016); AllWISE, R. M. Cutri et al. (2021) Tuch2024, N. W. Tuchow et al. (2024); Steph1986, C. B. Stephenson (1986); UHS, S. Dye et al. (2018).

3.2.2. Data Reduction

Data from both NIRSpec and MIRI were reprocessed using version 1.15.1 of the official JWST pipeline (H. Bushouse et al. 2022) using Calibration Reference Data System context file jwst_1322.pmap, with default parameters. We started from the unprocessed raw data downloaded from the Mikulski Archive for Space Telescopes (MAST). Corrections for cosmic rays, dark currents, count rate nonlinearity, bad pixel flagging, and other detector level corrections are applied to the raw data during stage 1 using the "calwebb_detector1" pipeline. The "calwebb_spec2" pipeline in stage 2 is then used with the data output from stage 1 to produce calibrated individual exposures. The individual exposures are combined in stage 3, where the final spectrum is extracted from the combined image. The final reduced data is presented in Section 5. All JWST data used in this paper can be found in MAST: 10.17909/rgey-0312.

3.3. Tull Coude Spectrograph

We observed BD+24 twice, first on 2024 July 13, and again on 2025 July 24, with the 2.7 m Harlan J. Smith Telescope, located at McDonald Observatory in Fort Davis, TX. Two stars from the stellar abundance catalog presented in J. M. Brewer et al. (2016), HD 131582 (spectral type K3) and HD 144872 (spectral type K3), were observed as abundance standards on 2025 April 12. Both abundance standards are similar brightnesses and colors as one another ($V = 8.608$ mag, $B - V = 0.993$ mag and $V = 8.61$ mag, $B - V = 0.96$ mag for HD 131582 and HD 144872, respectively), but slightly brighter and bluer than BD+24 ($V = 9.88$ mag, $B - V = 1.16$ mag). We used the Tull Coude Spectrograph in TS23 mode, with slit #4, grating E2, and the TK3 detector, resulting in continuous spectral coverage from 3500–10500 Å at a resolution of $R \sim 60{,}000$, achieving an average SNR of ∼200. The raw Tull Coudé Spectrograph data are initially processed using the Tull Coudé Spectrograph Data Reduction Pipeline (`TSDRP`[22]). This pipeline performs essential calibration and extraction steps, including bias subtraction, trace identification, scattered light subtraction, wavelength calibration, flat-field correction, cosmic-ray rejection, and spectral extraction for each spectral order. Additionally, TSDRP provides deblazing, continuum normalization, and order combination to produce a single, fully processed spectrum for each exposure. All spectra were then corrected for radial velocity shifts using `iSpec`'s cross-correlation

[22] https://github.com/grzeimann/TSDRP

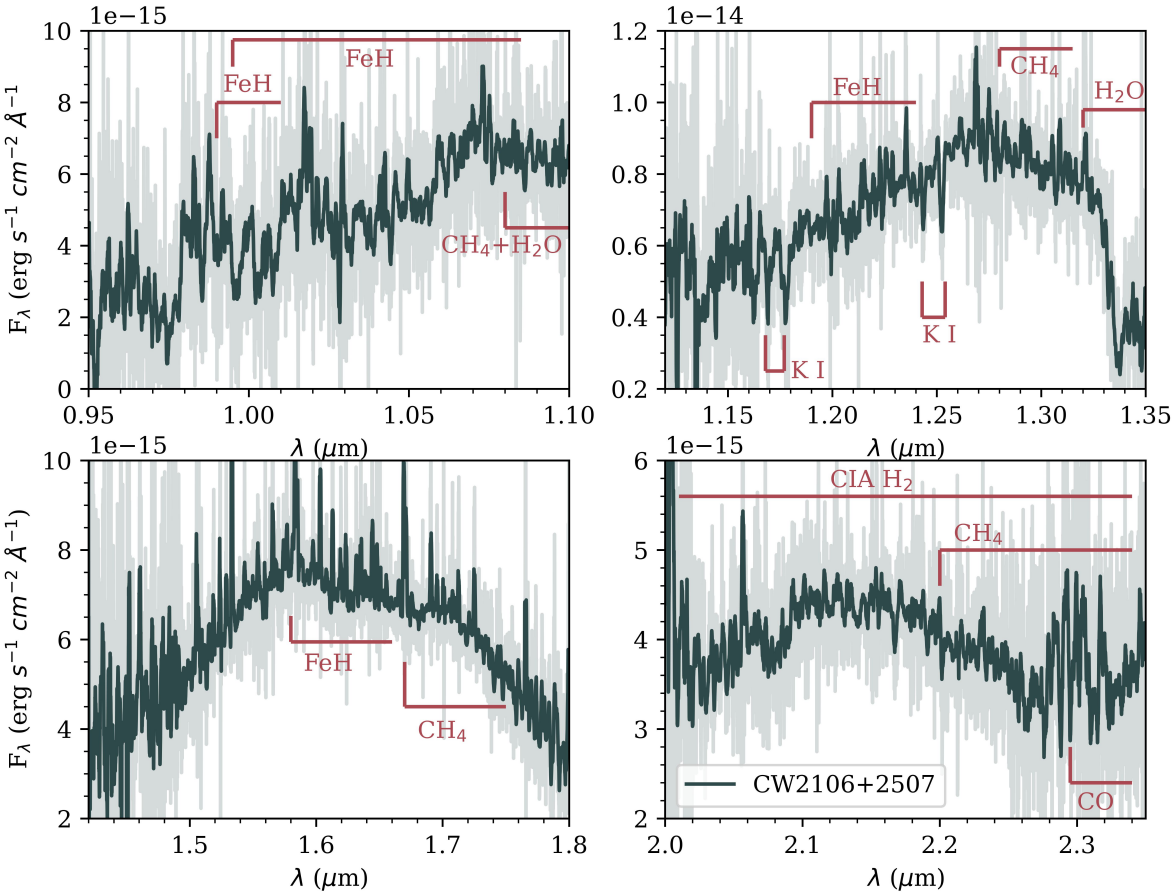


Figure 2. Magellan FIRE/Echelle spectrum of CW 2106 shown in gray, with the smoothed spectrum overplotted in dark green. Major absorption features have been labeled in each panel.

function with a NARVAL solar spectrum provided with the installation (S. Blanco-Cuaresma et al. 2014). Finally, all spectra of the same object were coadded, weighting by the signal-to-noise of each exposure. A portion of the spectrum of BD+24 is shown in Figure 3.

4. BD+24 4329 Characterization

The power of a benchmark system lies in utilizing well determined information on its host star. To properly utilize CW 2106 as a benchmark brown dwarf, it is crucial to fully understand its host, BD+24 4329. In this section, we provide a full characterization of BD+24 4329, estimating its age and deriving its elemental abundances.

4.1. Fundamental Parameters and Elemental Abundances

4.1.1. BACCHUS

We used version 72 of the Brussels Automatic Code for Characterizing High accUracy Spectra (BACCHUS; T. Masseron et al. 2016) to derive the fundamental parameters and elemental abundances for BD+24 and the two abundance standards from J. M. Brewer et al. (2016). BACCHUS is a line-by-line spectral fitting code that synthesizes spectra using the radiative transfer code TURBOSPECTRUM (B. Plez 2012) adopting the MARCS model atmosphere grid (B. Gustafsson et al. 2008) and assuming one-dimensional local thermodynamic equilibrium (1D LTE). Stellar parameters ($T_{\rm eff}$, log g, [M/H], microturbulent velocity, $v_{\rm mic}$) are determined using Fe ionization-excitation balance, where BACCHUS iterates until it finds the combination of parameter values that results in an agreement between the abundances measured from Fe I and Fe II lines and null trends between each Fe I line's measured abundance both the excitation potential and reduced equivalent width of that transition. Abundances are determined in a line-by-line way. For each line of each element, BACCHUS synthesizes five absorption lines with abundances that range from −0.6 dex to +0.6 dex centered on the expected abundance of the line assuming a solar abundance pattern scaled to the metallicity of the star. The abundance of each line is then determined using four methods (the χ^2, equivalent width, synthetic spectrum, and line intensity methods; see a detailed description in C. R. Hayes et al. 2022), and each method returns an associated flag reporting the quality of the measurement. Users can then include or exclude specific lines from their analysis by applying those flags. We adopt version 5 of the Gaia-ESO linelist for our atomic transition data (U. Heiter et al. 2021) and combine molecular transition data from numerous sources: CH from T. Masseron et al. 2014, C2, CN, OH, and MgH from T. Masseron, private communication (2018), SiH from R. L. Kurucz 1992, and TiO, FeH, and ZrO from B. Pelz, private communication (2018).

The choice of instrument, spectral fitting technique, model atmospheres, atomic data, and lines being measured all affect

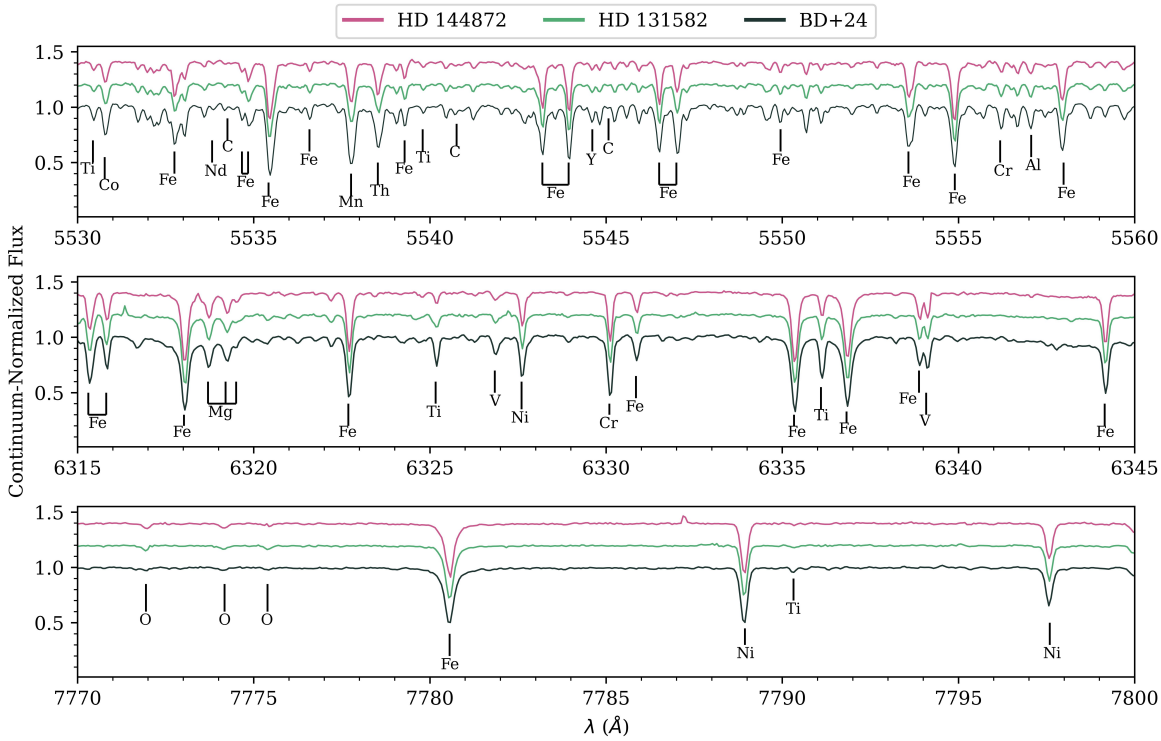


Figure 3. Subsets of BD+24's spectrum, as described in Section 3.3, in black along with the spectra of HD 131582 and HD 144872 as pink and green lines, respectively, all separated by a constant. Prominent absorption lines are labeled.

the parameters and abundances determined for a star (e.g., P. Jofré et al. 2019). A major goal of this work is to compare BD+24's parameters and abundances to those of typical disk stars in the J. M. Brewer et al. (2016) catalog. As such, we must adopt the same frame of reference as J. M. Brewer et al. (2016). To achieve this, rather than performing standard abundance analysis, which can, again, lead to global offsets between our results and those of J. M. Brewer et al. (2016) due to differences in methodology and data, we leverage the strictly line-by-line *differential* technique, anchoring ourselves to the two abundance standards also observed by J. M. Brewer et al. (2016) and thus the same parameter and abundance reference frame. This method has been used extensively in the literature to determine precise parameters and abundances for stars (e.g., J. Meléndez et al. 2012; F. Liu et al. 2014; J. Yana Galarza et al. 2016; H. Reggiani & J. Meléndez 2017; M. Bedell et al. 2018; L. Spina et al. 2018; M. McKenzie et al. 2022; D. Yong et al. 2023, and references therein). Strictly line-by-line differential analysis essentially determines how *different* a star is in, e.g., $T_{\rm eff}$, $\log g$, [M/H], $v_{\rm mic}$, and detailed elemental abundance ([X/H]) with respect to a chosen reference star. If we adopt the parameters and abundances reported by J. M. Brewer et al. (2016) for the two abundance standards, then we can add to them our differential results for BD+24 to get parameters and abundances in the same reference frame as J. M. Brewer et al. (2016), enabling direct comparison to their catalog while minimizing systematic offsets.

To determine line-by-line differential parameters and abundances for BD+24 with respect to our two abundance standards HD 131582 and HD 144872, we must first measure their line-by-line abundances. We adopt the stellar parameters reported by J. M. Brewer et al. (2016; see "Lit." column of Appendix Table A1) and use BACCHUS to measure Fe I, Fe II, and 24 other elemental abundances, only considering lines that the Gaia-ESO team report to be unblended in the Sun and Arcturus and have reliable atomic data (`synflag` = Y and `gfflag` = Y) and also that BACCHUS returns as unflagged in all four abundance measurement methods. Next, we solve for BD+24's parameters, once with respect to HD 131582 and again with respect to HD 144872, by performing differential Fe ionization-excitation with BACCHUS. Differential Fe ionization-excitation is similar to standard Fe ionization-excitation except that it requires a null trend between lines' excitation potentials and the line-by-line Fe I abundance *differences* between the star and its reference star. Similarly, it requires an agreement between the line-by-line Fe I and Fe II abundance differences between the star and its reference. Finally, we determine line-by-line abundance differences between BD+24 and the two abundance standards among all shared lines between the spectra.

Our approach returns two sets of differential abundances for BD+24, each of which is determined by taking the average of the line-by-line abundance differences between BD+24 and the reference star in each element and adding to them the abundances of the reference star reported by J. M. Brewer et al. (2016). Associated differential abundance uncertainties are determined by taking the quadratic sum of the standard deviation in the line-to-line abundance differences and the impact of each parameter's uncertainty on the resulting abundance.[23] Final elemental abundances for BD+24 are taken as the average of the abundances determined with respect to each reference star, weighted by the associated uncertainties, which are shown in Table 2. To validate our differential method, we also

[23] We determine the impact of each stellar parameter uncertainty on the resulting abundance by perturbing the model atmosphere by ± the parameter uncertainty and remeasuring abundances.

Table 2
BD+24 Derived Abundances and Parameters

Property	Δ_{131}[a]	Δ_{144}[b]	Final
$T_{\rm eff}$ (K)	4500 ± 79	4512 ± 21	4511 ± 21
log g (dex)	4.39 ± 0.05	4.50 ± 0.10	4.42 ± 0.05
[M/H] (dex)	0.00 ± 0.26	0.00 ± 0.06	0.00 ± 0.06
[Fe/H] (dex)	−0.05 ± 0.01	−0.01 ± 0.01	−0.03 ± 0.01
[C/H] (dex)	0.17 ± 0.02	0.16 ± 0.02	0.16 ± 0.02
[N/H] (dex)	−0.25 ± 0.05	−0.20 ± 0.05	−0.23 ± 0.04
[O/H] (dex)	0.11 ± 0.08	0.09 ± 0.09	0.11 ± 0.06
[Mg/H] (dex)	0.11 ± 0.03	0.08 ± 0.01	0.09 ± 0.01
[Si/H] (dex)	0.12 ± 0.07	0.19 ± 0.06	0.16 ± 0.04
[Ca/H] (dex)	0.03 ± 0.03	0.00 ± 0.03	0.02 ± 0.02
[Na/H] (dex)	−0.14 ± 0.10	⋯	−0.14 ± 0.10
[Al/H] (dex)	−0.03 ± 0.01	−0.09 ± 0.01	−0.06 ± 0.01
[Ti/H] (dex)	−0.08 ± 0.04	−0.05 ± 0.02	−0.06 ± 0.02
[V/H] (dex)	−0.02 ± 0.10	−0.07 ± 0.01	−0.07 ± 0.01
[Cr/H] (dex)	−0.08 ± 0.01	−0.09 ± 0.01	−0.09 ± 0.01
[Mn/H] (dex)	−0.09 ± 0.10	−0.12 ± 0.10	−0.11 ± 0.07
[Ni/H] (dex)	−0.02 ± 0.02	−0.02 ± 0.02	−0.02 ± 0.01
[Y/H] (dex)	⋯	−0.03 ± 0.10	−0.03 ± 0.10
C/O	0.63 ± 0.08	0.64 ± 0.09	0.63 ± 0.06
Mg/Si	1.00 ± 0.08	0.80 ± 0.06	0.87 ± 0.04

Notes.
[a] Differential values with respect to HD 131582.
[b] Differential values with respect to HD 144872.

determine differential parameters and abundances for each reference star with respect to the other reference star. The results of this validation are presented in Appendix A.

4.1.2. BD+24 Results

Figure 4 shows the abundances of BD+24 for several elements compared with stars from the Brewer catalog. Overall, the abundances of BD+24 are in decent agreement with the distribution seen in the Brewer Catalog. BD+24 does show evidence of slight enhancement in several elements compared to other solar metallicity objects, most notably [C/H], [Mg/H], and [Si/H], which lie above the bulk of the population. The [O/H] of BD+24 also appears to be slightly elevated, though the Brewer catalog shows a larger degree of scatter in [O/H] for a given [Fe/H], with BD+24 fitting well with the observed scatter. In contrast, the observed [N/H] of BD+24 falls on the lower end of the distribution, suggesting a possible minor depletion in N.

The C/O ratio of BD+24 is found to be more carbon rich than the bulk of the Brewer Catalog with C/O = 0.63 ± 0.06, where the median C/O of the Brewer Catalog is ∼0.47 with a maximum of 0.66 ± 0.07 (J. M. Brewer & D. A. Fischer 2016). The Mg/Si ratios of BD+24, in contrast, is slightly lower than the average Mg/Si of the Brewer Catalog, with Mg/Si = 0.87 ± 0.04 (compared with the median Mg/Si of 1.02 for the Brewer Catalog). However, J. M. Brewer & D. A. Fischer (2016) note that the distribution of Mg/Si is quite large, with ∼40% of the sample having an Mg/Si < 1.

4.2. System Age

In this section, we investigate multiple age indicators for BD +24, including kinematics, placement on CMDs, gyrochronology, and isochrones.

Using the full kinematics from Gaia DR3, we investigated any possibility of BD+24 belonging to a young moving group (YMG) using Banyan Σ (J. Gagné et al. 2018). Banyan Σ is a Bayesian algorithm that accepts as inputs the sky position, proper motions, radial velocity, and parallax of a source and compares its position and space velocities with those of 27 known YMGs. The output is a list containing the probability of belonging to each of the YMGs tested, as well as belonging to the field population (defined here as not belonging to any of the 27 YMGs). Using the values listed in Table 1, we get a probability of 99.9% of BD+24 4329 belonging to the field population, with all 27 YMGs having a probability of 0%. BD +24's placement on the Gaia CMD is in agreement with these results, as it appears to have an average luminosity for typical stars of its color, rather than being overluminous as is typically seen with younger stars.

The kinematics of BD+24 can also be used to calculate its projected orbit within the Milky Way. To do this we used the open-source code `galpy` (J. Bovy 2015), assuming a solar radius of 8 kpc and disk rotation speed of 220 km s^{-1} and using the `MWPotential2014` potential as described in J. Bovy (2015). This results in an orbit for BD+24 4329 with a periapsis of 7.16 kpc, an apoasis of 8.72 kpc, a maximum height above the plane of 0.07 kpc, and an eccentricity of 0.1 —all of which are consistent with an object belonging to the thin disk population, which has a scale height of $z = 300 \pm 50$ pc (J. Bland-Hawthorn & O. Gerhard 2016) and an eccentricity distribution that peaks at $e \sim 0.12$ (Y. Yan et al. 2019).

With no strong age constraints provided by the previously discussed age diagnostics, we used a hybrid dating technique that incorporates both isochrone fitting and gyrochronology. This was done using the open-source python package `stardate` (R. Angus et al. 2019). `stardate` uses a star's astrometric, photometric, spectroscopic, and rotational information, along with their associated uncertainties, to provide an age constraint through Markov Chain Monte Carlo sampling of the `MIST` evolutionary models (J. Choi et al. 2016; A. Dotter 2016). For the input parameters of BD+24 we used the astrometry and photometry from Gaia DR3, as well as photometry from 2MASS (M. F. Skrutskie et al. 2006) and the V magnitude from the Hipparcos input catalog (C. Turon et al. 1993). R. J. Oelkers et al. (2018) report a rotational period for BD+24 of $P_{\rm rot} = 30.42$ days, which we also used as an input for `stardate`. For the spectroscopic parameters, we used the log g, [Fe/H], and $T_{\rm eff}$ derived in Section 4.1. This provides a tight age constraint of $3.3^{+0.7}_{-0.5}$ Gyr. All other age diagnostics are consistent with this value, so we adopt the `stardate` derived age for BD+24.

5. CW 2106 Characterization

5.1. CW 2106 Spectral Type

To assign a spectral type to CW 2106, we first followed the approach of J. D. Kirkpatrick et al. (2010). The JWST/NIRSpec spectrum of CW 2106 was normalized to 1.28 μm and the spectral standards from J. D. Kirkpatrick et al. (2010) were overplotted and normalized in the same manner. The J bands of both CW 2106 and the standards were then visually compared. We found that both the L9 and T0 spectral standards fit the J band of CW 2106 equally well, making it difficult to discern between the two. Looking at the overall continuum, while the L9 provided the closest fit to CW 2106 in

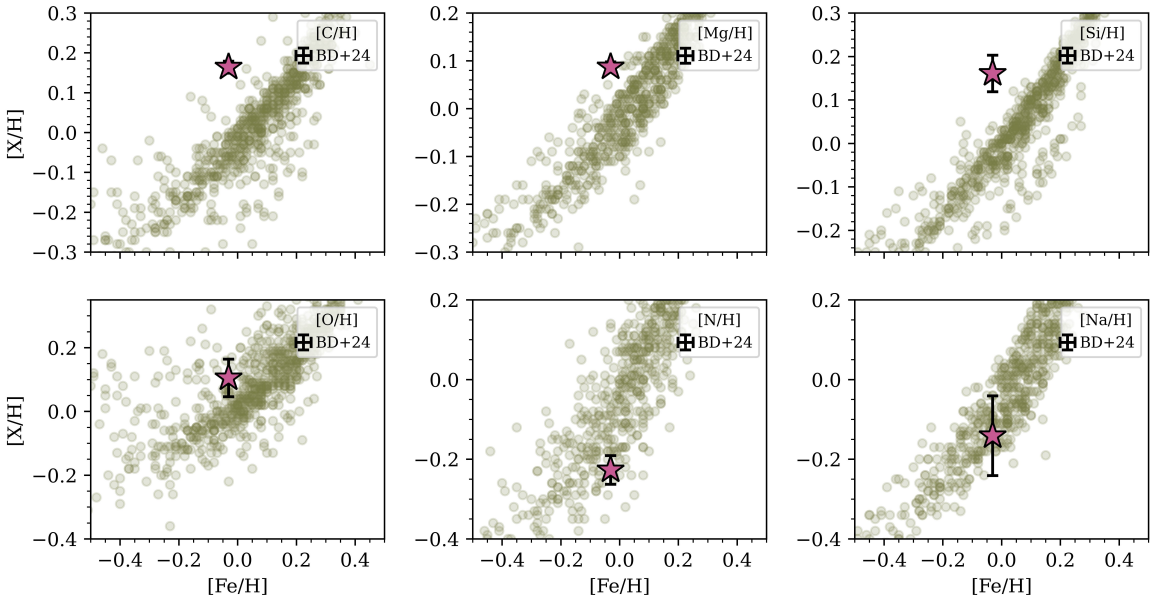


Figure 4. Abundances of select elements versus [Fe/H] for BD+24 (red star and error bars) along with the abundances of stars from J. M. Brewer et al. (2016; green points).

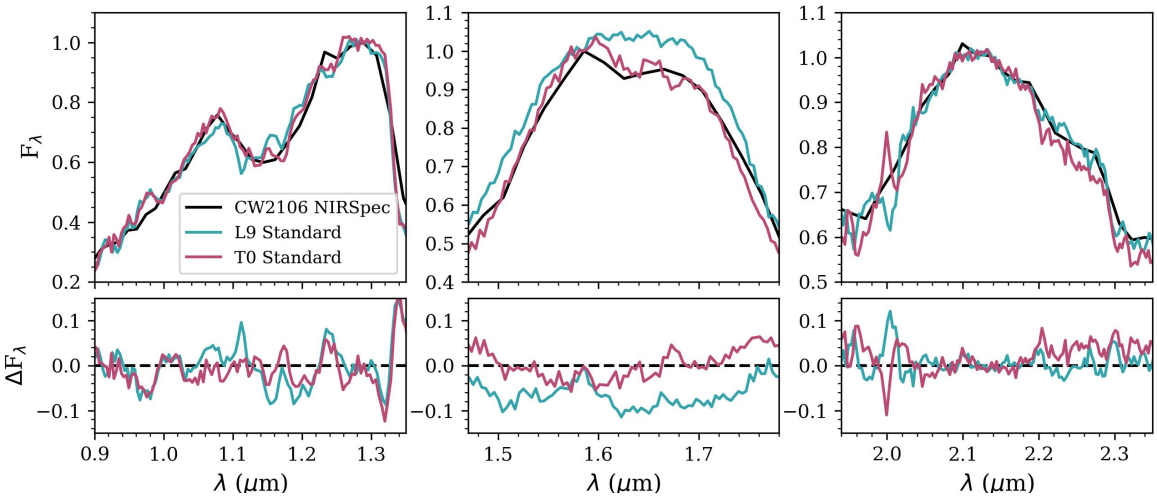


Figure 5. Top row: 0.9–2.35 μm near-IR spectrum of CW 2106 (black) along with the L9 (blue) and T0 (purple) standards, split into the *J* (left panel), *H* (middle panel), and *K* bands (right panel). Each spectrum was normalized to the peak of each respective band. Bottom row: residuals between CW 2106 and the L9 (blue) and T0 (purple) standards for the *J*, *H*, and *K* bands (left, middle, right panels respectively).

flux, the spectral morphology of CW 2106 appeared to more closely resemble that of the T0 standard.

To better help compare the spectral morphology of CW 2106, we next compared each of the *J*, *H*, and *K* bands separately, rather than the shape of the continuum. To do this, we cut each spectrum into the three individual bands, normalizing each to their respective peaks in flux. Figure 5 shows the normalized *J*, *H*, and *K* bands of CW 2106 compared to the L9 and T0 standards. While the *K*-band shape is better fit by the L9, the overall shapes of the *J* and *H* bands of CW 2106 are more similar to those of the T0 standard. We therefore assign CW 2106 a spectral type of T0 $\pm$ 1.

5.2. CW 2106 SED and Fundamental Parameters

We used the open-source code SEDkit (J. Filippazzo 2020; J. Filippazzo et al. 2025) in order to obtain the flux calibrated spectral energy distribution (SED) for CW 2016+2507. In this section, we summarize the methodology employed by SEDkit as well as present the SED and derived properties of CW 2106.

5.2.1. Construction of SED

In order to create an absolute flux calibrated SED and empirically derive bolometric luminosity ($L_{\rm bol}$), SEDkit follows the approach presented in J. C. Filippazzo et al. (2015). The first step is to provide SEDkit with any available spectra and their associated errors. For these we used the JWST NIRSpec/PRISM and MIRI/LRS spectra described in Section 3.2. In order to ensure the best quality data, we removed the detector edge portions of the NIRSpec and MIRI spectra (corresponding to SNR $<$ 5), resulting in continuous spectral coverage between 0.83 and 12.5 μm. A composite spectrum is then created using the average flux in their regions

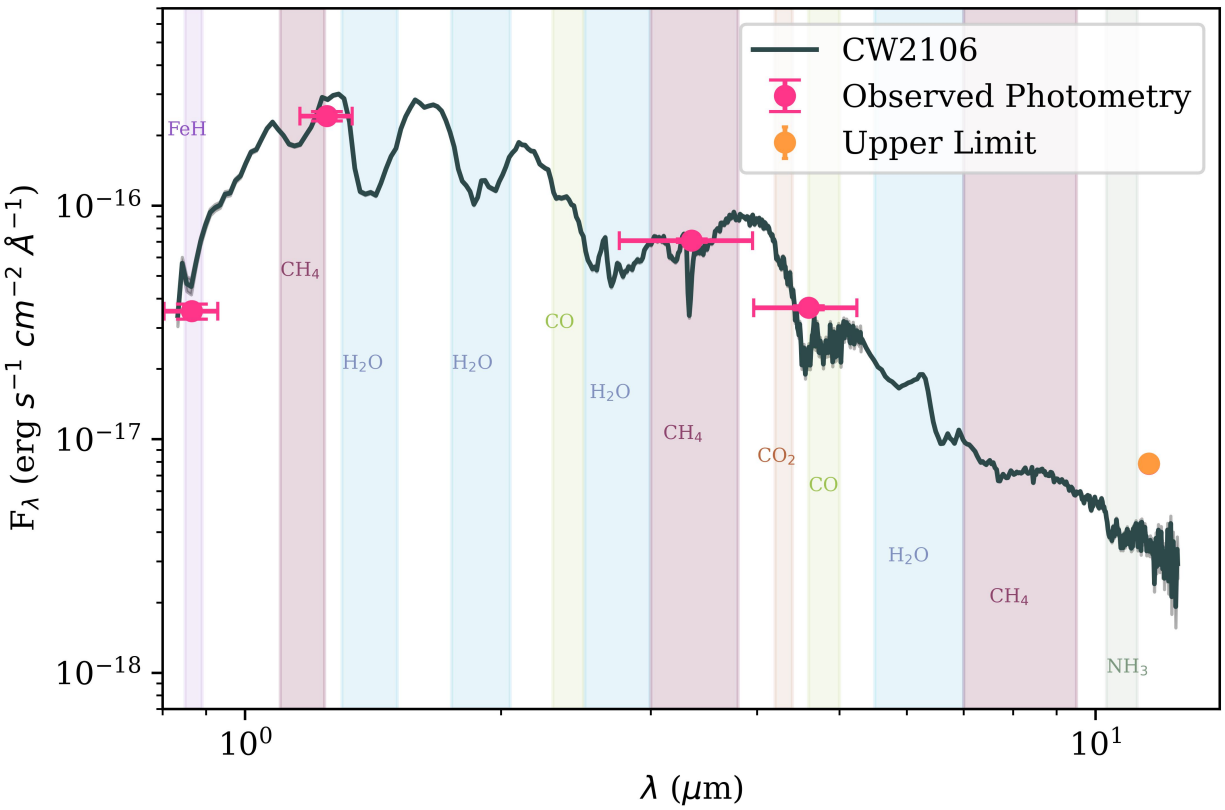


Figure 6. The Full (97.3%) JWST SED of CW 2106 shown in black. The observed photometry for CW 2106 (listed in Table 1) of CW 2106 are overplotted as pink points, with the associated flux errors and bandpass widths. Regions of broad molecular absorptions are highlighted and labeled.

of overlap, which for the NIRSpec/PRISM and MIRI/LRS spectra is between 4.9 and 5.5 μm. We also provided SEDkit with literature photometry (Table 1) for CW 2106. SEDkit then linearly interpolates from 0 μm to the shortest wavelength data point and appends a Rayleigh–Jeans tail from the longest wavelength data point out to 1000 μm.

Figure 6 shows the final, flux calibrated SED for CW 2106. The near-simultaneous, broad spectral coverage of CW 2106 provides an in-depth view of its atmosphere in a way not possible without JWST. For example, we can take a look at a similar object: SDSS J120747.17+024424.8 (J1207), a field dwarf of spectral type T0 (A. J. Burgasser et al. 2006). D. C. Stephens et al. (2009) presented the SED of J1207, which at the time was one of the broadest wavelength coverage SEDs for an L/T transition object. However, to achieve a similar spectral coverage to CW 2106, J1207 required the use of multiple ground- and space-based facilities, an observationally expensive endeavor, while still leaving several large gaps of wavelength. It should be pointed out that pre-JWST, assembling an SED as complete as J1207 was only possible for the brightest objects, leaving the majority of brown dwarf SEDs much more incomplete. The observations of J1207 were carried out over several years (SDSS—2001 July; UKIRT/CGS4 Z—2004 January; UKIRT/CGS4 J—2002 July; UKIRT/CGS4 H & K—2001 January; Gemini/NIRI—2005 April, May; Spitzer/IRS—2005 June) and, as brown dwarf atmospheres are dynamic, possibly cover different atmospheric conditions. The SED for CW 2106 from JWST is not plagued by these challenges, allowing for its atmosphere to be investigated under the same conditions and with no gaps in spectral coverage, highlighting just one way JWST will be able to help unlock the mysteries of these dynamic, enigmatic worlds.

5.2.2. Derivation of Fundamental Parameters

With the full flux calibrated SED created, SEDkit is then able to empirically derive the bolometric luminosity ($L_{\rm bol}$) for CW 2106. This is done using the equation:

$$L_{\rm bol} = 4\pi d^2 \int_{0\mu{\rm m}}^{1000\mu{\rm m}} F_\lambda d\lambda, \quad (1)$$

where d is the distance and F_λ is the absolute flux calibrated SED. For the distance of CW 2106, we adopted the Gaia DR3 distance of its host star of 34.11 $\pm$ 0.02 pc (Gaia Collaboration et al. 2023).

The derived $L_{\rm bol}$ is then used by SEDkit along with evolutionary models and a provided age range to estimate the object's mass, radius, and log g. The models chosen for this analysis were the evolutionary tracks of D. Saumon & M. S. Marley (2008, SM08), which model the L/T transition through use of a "hybrid" cloudy atmosphere prescription that linearly interpolates from a 1400 K cloudy atmosphere to a cloudless atmosphere at 1200 K. Model independent determinations of mass and luminosity for individual components of brown dwarf binaries have shown SM08 to be in excellent agreement with the data for objects within the L/T transition (i.e., T. J. Dupuy & M. C. Liu 2017). With a spectral type of T0 $\pm$ 1 (Section 5.1), CW 2106 falls right in the middle of the L/T transition and should therefore be best modeled by SM08.

For the age of CW 2106, we are once again able to turn to the host star and adopt the age for BD+24, which was

estimated in Section 4.2. The effective temperature ($T_{\rm eff}$) of CW 2106 was then calculated using the Stefan–Boltzmann Law:

$$T_{\rm eff} = \left(\frac{L_{\rm bol}}{4\pi R^2 \sigma_{SB}}\right)^{1/4}, \quad (2)$$

where R is the estimated radius of CW 2106, and σ_{SB} is the Stefan–Boltzmann constant.

Uncertainties were estimated using the spread of values derived repeating this analysis with the upper and lower bounds of the distance, age, and flux. A summary of all derived and estimated parameters for CW 2106 is shown in Table 1.

5.2.3. Comparison to Literature

With the fundamental parameters of CW 2106 now in hand, it is possible to see how it compares with other substellar objects. The spectral type of CW 2106 was found in Section 5.1 to be closest to T0 ± 1; previous studies have found field T0 dwarfs to have a $T_{\rm eff}$ of 1247 ± 113 K (J. C. Filippazzo et al. 2015) or 1190 ± 175 (A. Sanghi et al. 2023). The $T_{\rm eff}$ for CW 2106 in Section 5.2.2 of 1213± 21 K is consistent with these estimates, placing CW 2106 as typical for its spectral type.

Using the continuous, broad wavelength coverage from JWST, we are able to constrain our $L_{\rm bol}$ measurement to <0.5% uncertainty, adding it to the growing list of brown dwarfs observed by JWST with precise $L_{\rm bol}$ (e.g., S. A. Beiler et al. 2024). However, even with extremely precise $L_{\rm bol}$ measurements, S. A. Beiler et al. (2024) find that their uncertainty in $T_{\rm eff}$ is limited to 2.5%, a result of poorly constrained ages or radii. The benchmark nature of CW 2106 means that we are able to adopt a precise distance and age (therefore radius) via BD+24, overcoming this obstacle, and thus we are able to achieve an uncertainty in $T_{\rm eff}$ of ∼1.7%, a significant improvement over the typical error in $T_{\rm eff}$ of field L/T transition objects from previous works (∼9%; J. C. Filippazzo et al. 2015).

The mass of CW 2106 was estimated by A. Rothermich et al. (2024) to be ∼36 $M_{\rm Jup}$. This estimate was made using the phototype of CW 2106 in A. Rothermich et al. (2024; ∼T2) and the average mass per spectral type bin relation derived in T. J. Dupuy & M. C. Liu (2017) using objects with dynamical mass measurements, which placed CW 2106 within the T2-T5.5 bin with a mass of 36 ± 9 $M_{\rm Jup}$. In Section 5.1, we found that the spectral type of CW 2106 was T0 ± 1, which would actually place it within the T. J. Dupuy & M. C. Liu (2017) spectral type bin of L8-T1.5, which has a mass range of 34–62 $M_{\rm Jup}$. We derive for CW 2106 a mass range of 50–62 $M_{\rm Jup}$, consistent with the value from this new spectral type bin.

Figure 7 plots mass versus radius for CW 2106 and the F15 and S23 samples, colored based on assigned age, along with the SM08 evolutionary models. Also shown in Figure 7 are transiting brown dwarfs with similar masses and ages to CW 2106, who's properties have been independently determined. This comparison shows that while CW 2106 has a smaller radius than the bulk F15 and S23 samples, this is largely due to the lack of constrained ages for these objects. When only looking at the F15 and S23 objects with ages, CW 2106 becomes less of an outlier, falling in line with the expected radii for objects >1 Gyr as indicated by the evolutionary model tracks. Figure 7 also shows the derived radius of CW 2106 is in good agreement with the independently measured radii from the transiting brown dwarfs.

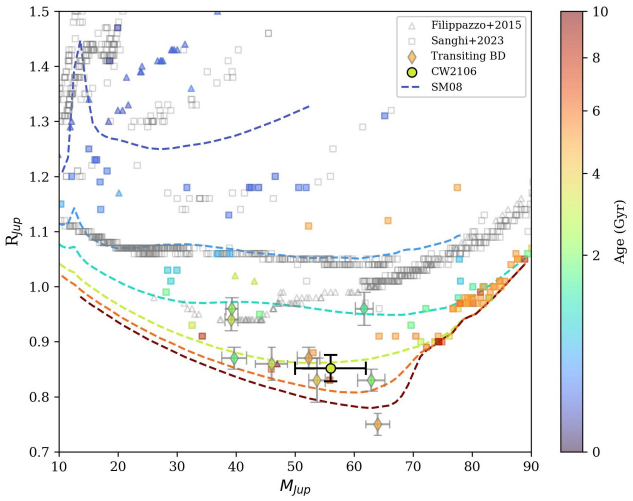


Figure 7. $M_{\rm Jup}$ vs. $R_{\rm Jup}$ for the sample from J. C. Filippazzo et al. (2015; F15, triangles), the sample from A. Sanghi et al. (2023; S23, squares), and CW 2106 (circle). Also shown as diamonds are the transiting brown dwarfs WASP-128b (V. Hodžić et al. 2018), CWW 89Ab (G. Nowak et al. 2017), KOI-205b (R. F. Díaz et al. 2013), TOI-1406b (T. W. Carmichael et al. 2020), EPIC 212036875b (T. W. Carmichael et al. 2019; C. M. Persson et al. 2019), TOI-852b (T. W. Carmichael et al. 2021), WASP-30b (D. R. Anderson et al. 2011), LHS 6343C (J. A. Johnson et al. 2011), and TOI-569b (T. W. Carmichael et al. 2020), using the updated values presented by T. W. Carmichael (2023). Overplotted as dashed lines are the evolutionary models of D. Saumon & M. S. Marley (2008, SM08). All points and lines are colored by their assigned age as indicated by the colorbar, or if no age constraint is present, points are left as empty gray outlines.

6. Spectral Analysis

In this section, we present an analysis of the spectral features of CW 2106 using the Magellan/FIRE, NIRSpec/PRISM, and MIRI/LRS spectra. We divide our discussion into three main sections: (i) the 0.8–2.5 μm portion of the near-IR (the "classical" near-IR), (ii) the 2.5–5 μm portion of the near-IR (uniquely obtained from state-of-the-art space-based observatories, referred to from this point as the near/mid-IR), and (iii) the mid-IR from 5–12.5 μm.

6.1. 0.8–2.5 μm

Figure 8 shows the 0.8–2.5 μm near-IR spectrum of CW 2106 from NIRSpec/PRISM, along with the absorption cross sections for the major absorbers expected (shown for $T_{\rm eff}$ = 1200 K at 1 bar) to exist within its atmosphere. Prominent water (H_2O) and methane (CH_4) absorption features dominate this region of the spectrum, sculpting the continuum into four distinct peaks at 1.08, 1.27, 1.59, and 2.07 μm as is typical for this spectral type (A. J. Burgasser et al. 2002b; J. D. Kirkpatrick 2005). Also visible is the carbon monoxide (CO) feature at 2.3 μm, and a large feature at 0.87 μm due to a combination of chromium hydride (CrH) and iron hydride (FeH).

Another weaker CrH+FeH feature at 0.97 μm can be seen in the FIRE/Echelle spectrum (Figure 2). Figure 2 also labels the K I doublets at ∼1.17 and 1.25 μm. While they are visible in the FIRE/Echelle spectrum, the features are very weak. The

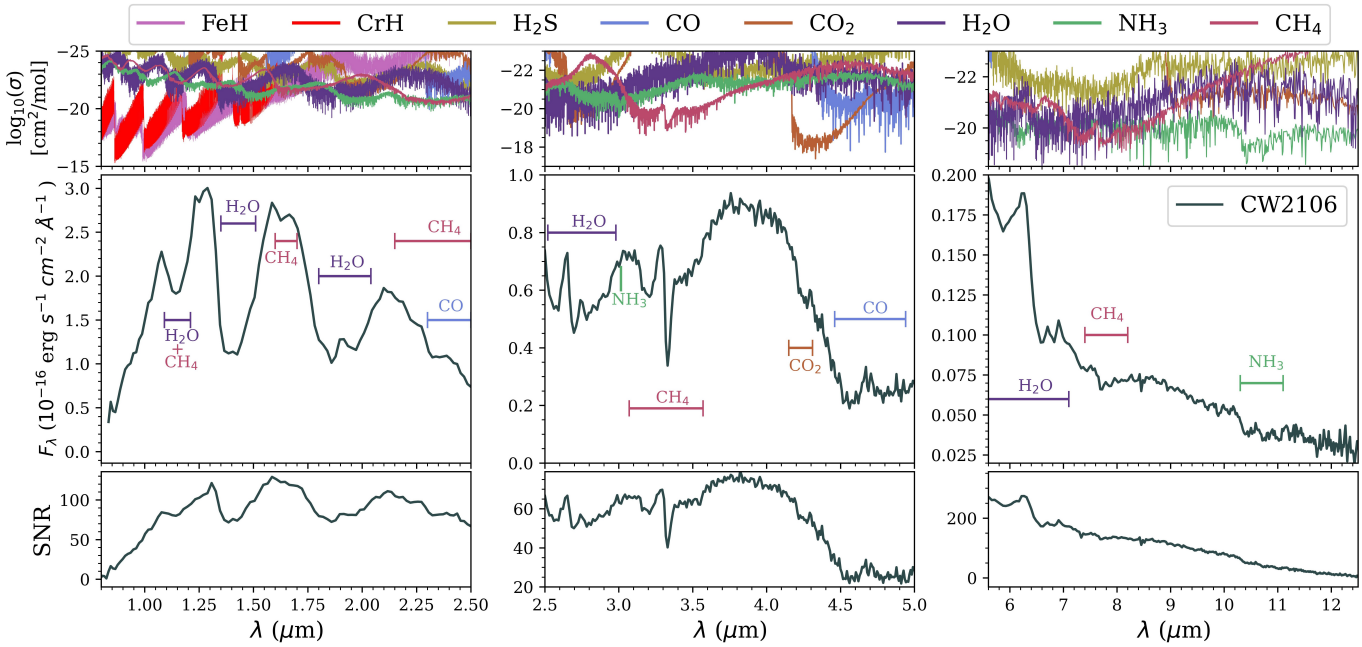


Figure 8. Left: absorption cross sections for several gasses common in brown dwarf atmospheres taken from C. E. Hood et al. (2024) and references within (top panel). Cross sections are shown for $T_{\rm eff} = 1200$ K and a pressure of 1 bar. The 0.8–2.5 μm NIR region of the JWST/NIRSpec spectrum for CW 2106 shown in the middle panel in black. Broad molecular absorption features are labeled in the same color as their respective cross sections. The corresponding SNR of CW 2106 is shown in the bottom panel. Middle: same as the left, but for 2.5–5 μm near/mid-IR. Right: same information shown for the mid-IR (5–12.5) μm.

spectrum is visibly very noisy, so the weak lines may be due to the low SNR of the data more-so than an inherent property of CW 2106. K I strength has been found to be correlated with surface gravity for late-M and L-dwarfs (e.g., M. R. McGovern et al. 2004), where the strengths of the lines decrease with decreasing surface gravity. However, G. Suárez et al. (2021) found that K I strength is no longer a reliable indicator of surface gravity once into the early-T spectral types (∼T2–T3). If the observed K I strengths of CW 2106 are reliable, however, its weak lines plus high surface gravity (log $g \sim 5.28$ dex) would indicate that this lack of correlation with surface gravity could possibly begin as early as spectral type T0. Future higher spectral resolution observations of CW 2106 will be able to help determine the strengths of its K I doublets, constraining their behavior during a critical transition point in brown dwarf evolution.

6.2. 2.5–5 μm

The 2.5–5 μm portion of CW 2106's NIRSpec/PRISM spectrum is shown in Figure 8 with the absorption cross sections for the expected major absorbers. Several striking features are observed including broad H_2O at ∼2.7 μm, the 3.3 μm fundamental CH_4 band, carbon dioxide (CO_2) at 4.2 μm, and the 4.6 μm fundamental CO band.

We also tentatively identify the 3 μm ν_3 NH_3 band first identified by S. A. Beiler et al. (2023) and confirmed by S. A. Beiler et al. (2024), which analyzed the spectra of 23 late-T and -Y dwarfs (ranging from $T_{\rm eff} \sim 1000$ to 350 K). While the proposed feature in CW 2106 lines up with the increase of NH_3 opacity from the absorption cross sections in Figure 8 and agrees with what is seen in S. A. Beiler et al. (2024), we cannot confirm this detection due to its low strength. S. A. Beiler et al. (2024) found the depth of the ν_3 NH_3 band increased with decreasing $T_{\rm eff}$ in the majority of their sample, so if confirmed in CW 2106, its warmer $T_{\rm eff}$ (1213± 21 K) and shallower absorption depth would agree with this trend. Future observations at a higher spectral resolution may help to confirm this detection.

6.3. 5–12 μm

Figure 8 shows the 5–12 μm MIRI/LRS spectrum for CW 2106. The Spitzer IRS sample from G. Suárez & S. Metchev (2022) shows that for objects of a similar spectral type to CW 2106 (T0 ± 1) this region is dominated mainly by prominent absorption features of H_2O and CH_4. These features are clearly seen in the MIRI/LRS spectrum of CW 2106 and have been labeled in Figure 8. Also visible in the MIRI/LRS spectrum is the 10.5 μm NH_3 feature. G. Suárez & S. Metchev (2022) found that NH_3 became detectable as early as spectral type T1.5 in their IRS sample; however, CW 2106 is a whole subtype earlier. One potential explanation for the lack of NH_3 at earlier spectral types in the IRS sample for spectral types <T1.5 is the low SNR of the Spitzer spectra. The median SNR of the spectra in G. Suárez & S. Metchev (2022) is ∼20 at 6 μm and ∼10 at 12 μm. While the MIRI/LRS spectrum also has an SNR of ∼10 at 12 μm, its SNR at 6 μm is closer to ∼250. This increase in SNR may explain the detection of NH_3 in CW 2106, and future JWST observations of similar type objects may be able to confirm whether or not the 10.5 μm NH_3 feature is common at this spectral type.

We find no evidence of the ∼8–11 μm silicate absorption feature for CW 2106 in Figure 8. G. Suárez & S. Metchev (2022) found using the Spitzer IRS sample that the onset of the silicate feature in field dwarfs is around spectral type L2, peaks around L4–L6, and is last detected at L8. In young brown dwarfs, clouds have been inferred as late as T2.5 with retrieval modeling (e.g., J. M. Vos et al. 2023), likely due to lower surface gravity allowing clouds to form higher up in the atmosphere. The strength of the silicate feature has also been found to strongly depend on the observed inclination angle (G. Suárez &

S. Metchev 2023), with equator-on objects displaying a stronger silicate absorption than objects viewed pole-on. At spectral type T0 $\pm$ 1 with an age of $3.3^{+0.7}_{-0.5}$ Gyr, it is not surprising CW 2106 lacks a noticeable silicate feature, especially if it is at a more pole-on inclination, following the trend observed in older field dwarfs.

6.4. Spectral Indices

We calculated the CH_4, NH_3, and H_2O indices as defined by M. C. Cushing et al. (2006) for CW 2106 using its MIRI LRS spectrum, allowing for a quantitative comparison of its spectral features discussed in Section 6.3 with those observed in the broader population. These indices focus on the 6.25 μm H_2O bands, the 8.5 μm CH_4 band, and the 10.5 NH_3 band.

For the calculations, we followed the approach of G. Suárez & S. Metchev (2022), which modifies the CH_4 index to focus on the 7.65 μm region rather than 8.5 μm, as well as defining an index for the silicate absorption feature centered around 9 μm. These indices are defined as:

$$H_2O\ \text{Index} = \frac{F_{6.25}}{0.562F_{5.8} + 0.474F_{6.75}} \quad (3)$$

$$CH_4\ \text{Index} = \frac{F_{10.0}}{F_{7.65}} \quad (4)$$

$$NH_3\ \text{Index} = \frac{F_{10.0}}{F_{10.8}} \quad (5)$$

$$\text{Silicate Index} = \frac{C_{9.3}}{F_{9.3}}, \quad (6)$$

where F_λ is the average flux around the specified wavelength, using a window of 0.3 μm for the H_2O index and 0.6 μm for CH_4, NH_3, and the silicate index. C_λ is defined in G. Suárez & S. Metchev (2023) as the average flux of a continuum assuming an exponential interpolation between 7.5 and 13.5 μm. However, we chose to use 11.5 μm versus 13.5 μm as the red end of the interpolation, as the SNR of the MIRI/LRS data drops significantly beyond $\sim$12 μm. Errors were computed using the errors of the the average flux in each window. The indices are designed such that values >1 indicate the presence of the molecule as long as the molecule feature region is not affect by other spectral features, with larger values indicating a stronger absorption feature.

Figure 9 shows the H_2O, CH_4, NH_3, and silicate indices versus spectral type for CW 2106 compared to the Spitzer IRS sample from G. Suárez & S. Metchev (2022). The higher SNR provided by JWST allows for more precise molecular indices than what was possible for most Spitzer observations. This is noticeable in Figure 9, with perceptibly smaller error bars for CW 2106 over the IRS sample, highlighting the power of JWST to better characterize and constrain the properties of brown dwarfs.

Comparing CW 2106 with objects of a similar spectral type, the H_2O index appears near normal for its spectral type. The CH_4 index for CW 2106 is slightly elevated, although the spread of CH_4 indices of L/T transition objects is quite large. CW 2106's NH_3 index also appears to be slightly higher than objects of a similar spectral type, though agrees within the error bars. Consistent with similar type objects from the Spitzer IRS sample, the silicate index for CW 2106 indicates the lack of a silicate absorption feature. This is in agreement with the lack of visual evidence for silicates in the mid-IR spectrum of C2106 in Section 6.3.

7. Comparison with Forward Models

In this section, we compare the full 0.8–12.5 μm SED of CW 2106 with a series of self-consistent atmospheric grid models encompassing both cloudy/cloudless atmospheres and equilibrium/disequilibrium chemistry. In order to do this, we used the open-source python code `SEDA`[24] (G. Suárez et al. 2021; Suarez et al. 2026, in preparation), which provides χ^2 minimization and nested sampling frameworks for comparing observed data to multiple different atmospheric model grids. We performed a χ^2 minimization over all of the model grids chosen (described below) in order to find the best fits.

In addition to finding the best model fits to the full SED, we also investigated the best-fitting models over three different wavelength ranges using those defined in Section 6: 0.8–2.5 μm (the "classical" near-IR), The 2.5–5 μm near/mid-IR, and 5–12 μm (the mid-IR). The near- and mid-IR originate in different layers of the atmosphere; lower pressures ($\lesssim$1 bar, B. Burningham et al. 2021) are probed by the mid-IR while the near-IR probes the hotter, deeper layers ($\sim$1–20 bar; T. Karalidi et al. 2021; A. M. McCarthy et al. 2024). Exploring which models best fit these different wavelengths therefore yields insight into the potential conditions present in different layers of the atmosphere.

7.1. Models Used

To perform the χ^2 minimization fits, we used three separate grid models covering different chemistry regimes and atmospheric parameters. Below we provide a brief description of the models used, their assumptions, and the parameter space covered. For a more detailed discussion of a specific model grid, we direct the reader to that model's cited paper.

7.1.1. `ATMO2020`

The `ATMO2020` atmospheric models (M. W. Phillips et al. 2020) are a set of three grids that assume solar metallicity and a cloudless atmosphere. Each grid includes a different regime of chemistry: (i) chemical equilibrium, (ii) nonequilibrium chemistry caused by weak vertical mixing, parameterized with by the eddy diffusion coefficient K_{zz} ($\log(K_{zz}) = 4$ dex), and (iii) nonequilibrium chemistry due to strong K_{zz} ($\log(K_{zz}) = 6$ dex). All three grids cover the range $T_{\rm eff} = 200$–3000 K (with steps of 100 K and 50 K for $T_{\rm eff} > 600$ K and $T_{\rm eff} < 600$ K respectively) and $\log g = 2.5$–5.5 dex (with steps of 0.5 dex).

7.1.2. `Sonora Elf-Owl`

The `Sonora Elf-Owl` atmospheric models were developed by S. Mukherjee et al. (2024) as part of the Sonora family of models. This model assumes a cloudless atmosphere and disequilibrium chemistry due to vertical mixing and takes into account the effects of changing metallicity and C/O ratio. The `Elf-Owl` grid spans the parameter space $T_{\rm eff} = 275$–2400 K, $\log g = 3.25$–5.5 dex, $\log(K_{zz}) = (2,4,7,8,9)$ dex, [M/H] = (−1.0, −0.5, 0.0, +0.5, +0.7, +1.0) dex, and C/O = (0.22, 0.458, 0.687, 1.12). The $\log g$ varies by 0.25 dex and the $T_{\rm eff}$ varies by 25 K between 275–600 K, 50 K between 600–1000 K, and 100 K between 1000 and 2400 K.

[24] https://seda.readthedocs.io/en/latest/index.html

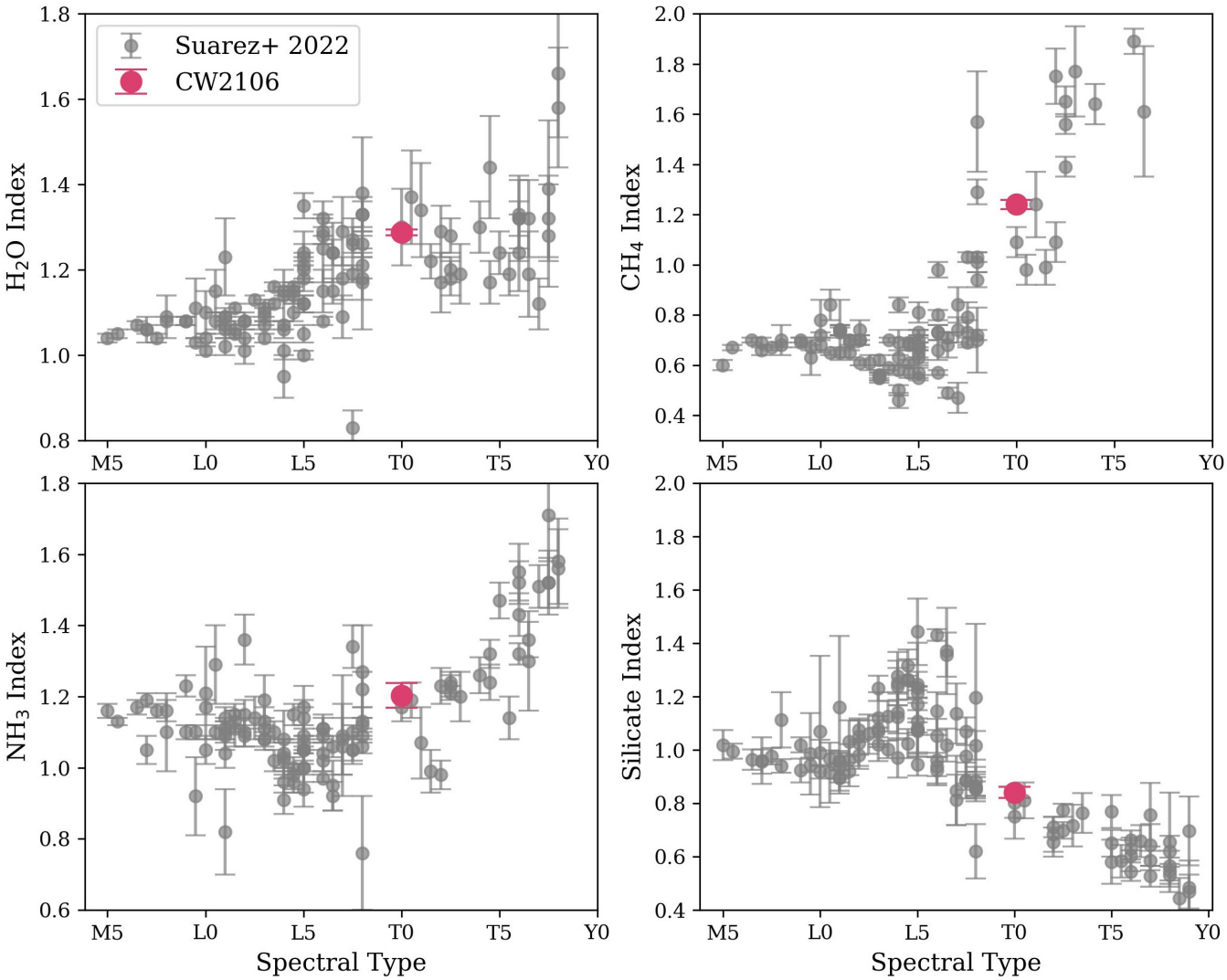


Figure 9. Molecular indices as defined in Section 6.4 vs. spectral type. CW 2106 is shown as a red circle, with the SPITZER IRS sample from G. Suárez & S. Metchev (2022) shown as gray circles.

7.1.3. `Sonora Diamondback`

Another in the Sonora family of models, `Sonora Diamondback` (C. V. Morley et al. 2024) is a grid of atmospheric models under chemical equilibrium that include the effects of clouds at three different metallicities. Cloud species included are enstatite ($MgSiO_3$), forsterite (Mg_2SiO_4), aluminum oxide (Al_2O_3), and iron (Fe), with varying thickness for all species (controlled by the parameter f_{sed}). The `Diamondback` models span the parameter space T_{eff} = 900–2400 K (ΔT_{eff} = 100 K), log g = 3.5–5.5 dex (Δlog g = 0.5 dex), [M/H] = (−0.5, 0.0, +0.5) dex, and f_{sed} = (1, 2, 3, 4, 8, nc), where "nc" indicates a cloudless atmosphere. All models are assumed to have a solar C/O.

7.2. Results

7.2.1. Full SED Fit

Figure 10 shows the best-fit models from each of the model families used for each of the four wavelength ranges compared (0.83–2.5 μm, 2.5–5 μm, 5–12.5 μm, and 0.83–12.5 μm) along with the SED of CW 2106. Over the full 0.8–12 μm SED (bottom panel of Figure 10), the `Sonora Diamondback` cloudy model (solid line) offers a significantly better fit over the cloudless `ATMO2020` (dotted line) and `Elf-Owl` (dashed line). The preferred `Diamondback` model has a T_{eff} = 1300 K, log g = 3.5 dex, [M/H] = 0.0 dex, and f_{sed} = 4. While this may be the best-fitting model out of all of those compared (χ^2 = 109.2 versus 664.3 and 889.6 for `Elf-Owl` and `ATMO2020` respectively), visual inspection of the comparison shown in the bottom panel of Figure 10 shows that it is still a relatively poor fit to the data, particularly in the near-IR. The J and H bands of the `Diamondback` model are underluminous when compared with the observed flux from CW 2106, whereas the model is overluminous in the ∼2.2–3 μm region. The `Diamondback` model also fails to capture the shape of the 4 μm peak and the depth of the 4.6 μm CO band absorption. The mere existence of CO in most brown dwarf atmospheres indicates a deviation from equilibrium molecular abundances (e.g., K. S. Noll et al. 1997; D. Saumon et al. 2006; S. Sorahana & I. Yamamura 2012), so the lack of disequilibrium chemistry in the `Diamondback` models may be responsible for this mismatch.

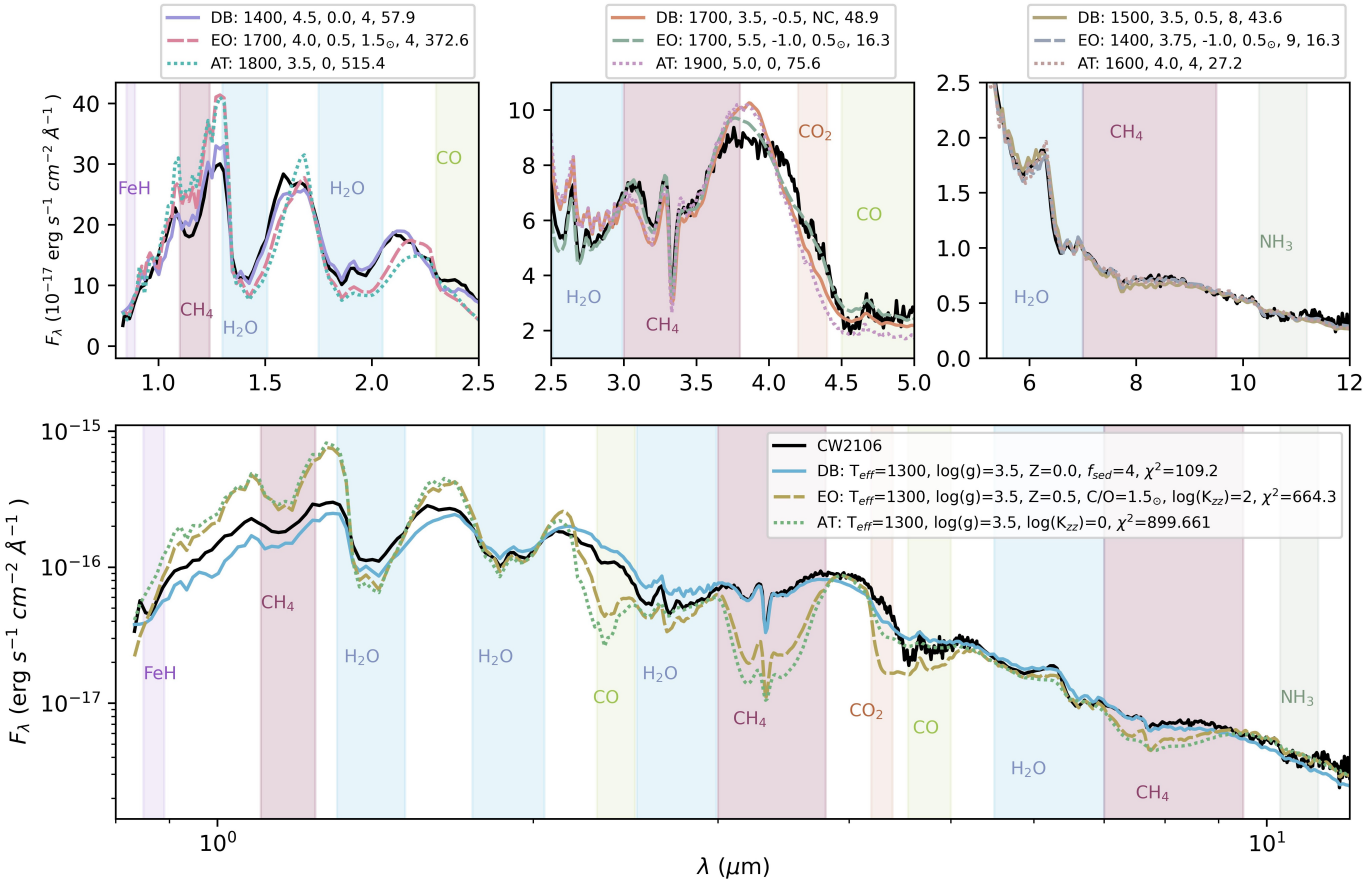


Figure 10. The SED of CW 2106 (solid black line) plotted with the best-fitting `Sonora Diamondback` (SD; colored solid line), `Sonora Elf-Owl` (EO; colored dashed line), and `ATMO2020` (AT; colored dotted line) models. Regions of broad molecular absorptions are highlighted and labeled. The best fits to the 0.80–2.5 μm, 2.5–5 μm, and 5–12 μm regions are shown in the left, middle, and right panels of the top row, with the bottom panel showing the best fits to the full SED. Model parameters are given in the same order as in the bottom panel: for SD—[$T_{\rm eff}$, log g, [M/H] (Z), $f_{\rm sed}$, χ^2]; For EO—[$T_{\rm eff}$, log g, [M/H] (Z), C/O, log(K_{zz}, χ^2]; For AT —[$T_{\rm eff}$, log g, log(K_{zz}), χ^2].

The parameters of the best-fitting `Elf-Owl` and `ATMO2020` models are similar to those of the `Diamondback` model; the only difference being the metallicity of the `Elf-Owl` model as [M/H] = 0.5 dex (versus the `Diamondback` metallicity of [M/H] = 0.0 dex). Both the `Elf-Owl` and `ATMO2020` fits favor a low vertical mixing rate, with log(K_{zz}) = 2 dex and 0 dex (i.e., chemical equilibrium), respectively. Visual inspection of the fits in Figure 10 (as well as their χ^2 values) confirms that the `Elf-Owl` and `ATMO2020` models do not adequately fit the observed data for CW 2106 to the same degree as the `Diamondback` model. While the `Elf-Owl` and `ATMO2020` model fits are less favored than those from `Diamondback`, all three models agree on a $T_{\rm eff}$ of 1300 K, not very far from the value derived in Section 5.2.2 ($T_{\rm eff}$ = 1213 K). This highlights the importance of obtaining broad wavelength coverage for the estimation of $T_{\rm eff}$, as model fits to smaller wavelength regions (see Section 7.2.2) show a wide variance of $T_{\rm eff}$ depending on the model and wavelength region choices.

The preference for the cloudy `Diamondback` model is suggestive for the need of clouds in the atmosphere of CW 2106 to explain its SED. While CW 2106 lacks the 9 μm silicate feature (Section 6), its placement on the CMD in Figure 1 shows its colors are more similar to those to the cloudy L-dwarfs than those of the cloudless T-dwarfs. Hence, the interpretation of a cloudy atmosphere for CW 2106 from the `Diamondback` fit is in agreement with the observed data.

7.2.2. Fits by Region

Looking at the best fits for each of the chosen regions in the top three panels of Figure 10 shows a large degree of variance in the obtained parameters, both from the full SED model fits as well as between each region. These inconsistencies suggest that relying on any one small wavelength range may lead to incorrect results, as those analyses would be missing crucial spectral features that lie outside of that range. Instead, the consistent parameters between each of the models when compared to the full SED of CW 2106 point toward the need for broad wavelength coverage in order to confidently infer an object's fundamental parameters. While the parameters such as $T_{\rm eff}$ and log g for the individual fits in each region may not be consistent, by comparing which model grid (and their different atmospheric assumptions) better fits the spectral features of CW 2106, it may be possible to draw rough inferences as to the possible conditions at different depths within its atmosphere.

Figure 10 shows that the `Diamondback` model provides a significantly better fit (χ^2 = 57.9) to the 0.83–2.5 μm range of CW 2106 over the cloudless `Elf-Owl` (χ^2 = 372.6) and `ATMO2020` (χ^2 = 515.4) models. This is consistent with the fits to CW 2106's full SED, and likewise points to the need for

clouds to explain the morphology of CW 2106's near-IR spectrum. The fits to the 2.5–5 μm wavelength range tell a different story. Here, the best-fitting model is from the cloudless `Elf-Owl` grid ($\chi^2 = 16.3$), followed by the `Diamondback` model ($\chi^2 = 48.9$) but with no clouds. The 5–12.5 μm mid-IR portion of CW 2106's SED is similarly fit better by the cloudless models.

The preference for cloudless models with the mid-IR wavelengths (which probe atmospheric pressures $\lesssim$1 bar) but the cloudy model in the near-IR (which probes pressures $\sim$1–20 bar) suggests that clouds are only present in the deepest visible layers of CW 2106's atmosphere. As an L/T transition object, this may be evidence of the cloud sedimentation process ongoing within CW 2106's atmosphere, having not yet rained out below the photosphere.

8. Silicate Clouds

8.1. Clouds: A Quick Overview

Early observations of L-type brown dwarfs in the near-IR found that their significantly reddened colors were best explained by "dusty" atmospheres, which were host to both solid and liquid condensate species (e.g., J. D. Kirkpatrick et al. 1999, 2000; G. Chabrier et al. 2000; A. S. Ackerman & M. S. Marley 2001). These observations were in agreement with theoretical models, which predicted that by the effective temperatures of mid-L dwarfs, species such as liquid iron and magnesium silicates (e.g., SiO_2, $MgSiO_3$, Mg_2SiO_4) have formed within the observable atmosphere (K. Lodders & B. Fegley 2006). These clouds act as an opacity source, which blocks some of the light from deep within the atmosphere (observed primarily in near-IR wavelengths), redistributing the energy to longer wavelengths and resulting in a reddened SED.

While redder than normal near-IR colors of brown dwarfs served as an indirect proxy for "cloudiness," it was not until the launch of the Spitzer Space Telescope (M. W. Werner et al. 2004) that the first direct observational evidence of clouds was possible. Through an analysis of the 5–14 μm spectra of M-, L-, and T-dwarfs from Spitzer, M. C. Cushing et al. (2006) were able to show for the first time a prominent absorption feature from $\sim$9–11 μm that was not predicted by atmospheric models at the time. This feature was speculated to be due to absorption from the Si-O stretching vibration mode of solid silicate grains, particularly small grains ($<$2 μm) high in the atmosphere.

G. Suárez & S. Metchev (2022) reanalyzed the entire M5-T9 Spitzer spectral sample, investigating the observed 9 μm silicate feature as a function of spectral type. This analysis found that the first appearance of the silicate feature is around spectral type L2 ($T_{\rm eff} \approx 2000$ K). The silicate feature then peaks in strength around L4–L6 ($T_{\rm eff} \approx$ 1700–1500 K), and disappears after spectral type L8 ($T_{\rm eff} \approx 1300$ K). Below this temperature, the clouds have sedimented to deeper layers of the atmosphere at higher pressures than those probed by mid-IR spectra ($\lesssim$1 bar).

While the silicate feature in spectral type T0 and later has yet to be identified with any significance, cloud effects can still be seen elsewhere in an object's SED, particularly in the near-IR, which probes the deeper pressures in which the clouds now sit. In addition to those that show redder than normal SEDs, several L/T transition objects have been found to be variable in the near-IR (e.g., J. Radigan 2014; S. C. Eriksson et al. 2019), thought to be driven by "patchy" clouds (A. J. Burgasser et al. 2002a).

J. M. Vos et al. (2023) investigated two such objects: SIMP J01365662+0933473 (T2.5, $T_{\rm eff} = 1150 \pm 70$ K) and 2MASS J21392676+0220226 (T1.5, $T_{\rm eff} = 1040 \pm 60$ K). Though both objects lack the 9–11 μm silicate feature, they are highly variable in the near-IR. J. M. Vos et al. (2023) modeled each object using the `BREWSTER` Retrieval framework (e.g., B. Burningham et al. 2017) to constrain both their cloud species, as well as their locations. They find that the data is best described by a patchy layer of Mg_2SiO_4 (located at 1.3–1.7 bar) above a deep iron cloud deck. Both objects investigated by J. M. Vos et al. (2023) are young ($\sim$200 Myr), and thus expected to be cloudier than their field-aged counterparts (G. Suárez & S. Metchev 2023). However, these objects are excellent case studies in how the presence of clouds can be inferred from observed spectra, even without the detection of the 9 μm silicate feature.

8.2. Is CW 2106 Cloudy?

The MIRI/LRS spectrum of CW 2106 shows a clear lack of the 9 μm silicate absorption feature, indicating that clouds (if present) are not significantly impacting the observable photosphere. However, the model fits performed in Section 7 showed that the cloudy `Sonora Diamondback` models best fit the observed SED of CW 2106 over the cloud-free `Sonora Elf-Owl` and `ATMO2020` models. CW 2106 is also slightly redder than a typical T0, with $J - W2 = 3.16 \pm 0.05$ compared to $J - W2 = 2.82 \pm 0.01$ (J. D. Kirkpatrick et al. 2021). These combined strongly suggest that CW 2106 does in fact have silicate clouds in its observable photosphere, causing shallower gas absorption features and a slightly reddened SED. So why then does CW 2106 lack a silicate feature?

One possible factor contributing to why CW 2106 may lack a silicate feature is its viewing angle. G. Suárez et al. (2023) investigated the strength of silicate features for brown dwarfs with known inclination angles. They found that objects viewed equator-on had stronger silicate features than those viewed closer to the poles (i.e., the equatorial latitudes of brown dwarfs are cloudier). While no inclination measurements exist for CW 2106 at this time, if CW 2106 is viewed more pole-on, this could help explain why no silicate feature is observed. However, this would not explain its slightly reddened SED, as objects viewed pole-on tend to have bluer than average near-IR colors (J. M. Vos et al. 2017; G. Suárez et al. 2023), nor would it explain the preference for cloudy models to explain the observed data.

Instead, the lack of a 9 μm silicate feature may be due to the evolutionary stage of CW 2106. As a T0 spectral type, CW 2106 sits directly in the middle of the L/T transition—an evolutionary stage defined by the clearing of clouds from the observable photosphere. This process is driven by the ever cooling atmosphere allowing individual condensate particles to grow in size until they are no longer buoyant and "rain out" to the deeper layers of the atmosphere. As a result, the cloud layer would be observed to effectively sink to deeper and deeper layers of the atmosphere throughout the L/T transition, up until the point in which the clouds are too deep to be observed, thereby leaving the observable atmosphere "cloud free." Taking another look at the model fitting performed in Section 7, when fitting the near- and mid-IR separately, while the near-IR was still best fit by the

cloudy model, the cloudless models were preferred for the fits to the mid-IR. This suggests that CW 2106 has a cloudy near-IR photosphere (primarily from deeper pressures of the atmosphere, ∼1–20 bar), but a cloudless mid-IR photosphere (pressures < 1), fitting the picture of an L/T transition object who's clouds have sedimented to the deeper layers of the atmosphere, but have not yet completely sunk below the observable photosphere.

8.3. Thermochemical Predictions

In Section 8.2, we discussed how the near-IR photosphere of CW 2106 likely hosts silicate clouds. There are several different species of silicate clouds that can form in a brown dwarf atmosphere, each removing different amounts of material from the observable photosphere, most importantly oxygen. Atmospheric retrievals on T-dwarfs have found an excess of supersolar C/O ratios (e.g., E. Calamari et al. 2022), explained as the result of oxygen being sequestered into various condensate species (A. Burrows & C. M. Sharp 1999; C. Visscher et al. 2010). Being able to characterize which cloud species have formed in an atmosphere, and therefore how much oxygen has been sequestered by silicate condensates, will allow us to better constrain how much oxygen sequestration is taking place into other condensate species (for example, into condensates of Ca, Ti, Al, and V).

E. Calamari et al. (2024) outline a thermochemical framework that predicts the species of silicate clouds that can form given a bulk composition, finding the strongest predictor to be the ratio between Mg and Si (Mg/Si). For systems with a bulk Mg/Si $\gtrsim$ 0.9, $MgSiO_3$ is the dominant silicate species, with increasing contributions of Mg_2SiO_4 as Mg/Si increases, until Mg/Si $\gtrsim$ 1.6 when Mg_2SiO_4 becomes the dominant condensate. In atmospheres with Mg/Si $\sim$ 0.9, only $MgSiO_3$ is predicted to form, while atmospheres with Mg/Si$\lesssim$0.9 also have an increasing contribution from SiO_2 as Mg/Si decreases further.

In Section 4.1.2, we derived an Mg/Si value for BD+24 of ∼0.87, which, as both objects form a dynamical pair, also applies to CW 2106. This value sits just at the 0.9 threshold identified by E. Calamari et al. (2024), suggesting that the most likely cloud species to form in the atmosphere of CW 2106 is $MgSiO_3$. Using this prediction, E. Calamari et al. (2024) provide a way of estimating the amount of oxygen being sequestered, denoted as "O_{sink}." For CW 2106, this value is $O_{sink} \approx 23\%$, meaning that around 23% of the bulk oxygen in CW 2106 is now locked into condensate clouds. The bulk C/O of BD+24 (and thus CW 2106) is ≈0.63; however, as 23% of the oxygen is removed from the gas phase in CW 2106, the atmospheric (i.e., observed) C/O ratio that is likely to be retrieved for CW 2106 will be skewed to the higher value of ∼0.82 due to the clouds sequestering the oxygen. Future retrievals will be able to affirm/refute this prediction and shed more light on the possible presence of $MgSiO_3$ within its atmosphere.

9. CW 2106 as a Benchmark

When attempting to estimate the parameters of isolated field dwarfs, it can be difficult to verify the trustworthiness of the results. To determine the validity of model parameters, it is necessary to compare the models with objects whose properties are already known. However, isolated brown dwarfs cannot be used to help improve model accuracy without "ground truth" values with which to correct to. CW 2106, as part of a benchmark system, is one of the few brown dwarfs whose composition and age are known via its well-characterized host star. This information, combined with high SNR broadband spectroscopic data from JWST, means that CW 2106 is well-poised to perform a direct test of the atmospheric models commonly used to estimate parameters of field objects. In Section 7, we fit three different forward model grids to CW 2106. Below we discuss some of the results of these model fits in context with the known parameters of CW 2106 from its host star.

9.1. T_{eff}

The best fit overall for the full SED of CW 2106 was the `Sonora Diamondback` model with $T_{\rm eff} = 1300$ K. Both the `Elf-Owl` and `ATMO2020` model best fits also had $T_{\rm eff} = 1300$ K. In Section 5.2.2, we derived a $T_{\rm eff}$ for CW 2106 of 1213 ± 21 K using its semiempirically measured $L_{\rm bol}$ along with an estimated radius using evolutionary models combined with the age of its host star. While similar, the $T_{\rm eff}$ of the models are ∼100 K hotter than that of CW 2106, although the step size of the model grids is also 100 K.

9.2. log g

The log g values for the best-fit models are all very low, with values of 3.5 for the `Diamondback`, `Elf-Owl`, and `ATMO2020` models. These log g values taken at face value would indicate that CW 2106 is a very young brown dwarf. For example, using the evolutionary models of D. Saumon & M. S. Marley (2008), an object with a $T_{\rm eff}$ of ∼1200 K and log $g = 3.5$ dex would be < 10 Myr old. Visually, the spectrum of CW 2106 shows no obvious signatures of low gravity that would lead us to believe it is actually young, such as the triangular shaped H-band continuum shape (e.g., K. N. Allers & M. C. Liu 2013). Likewise, we know the age of the system to be $3.3^{+0.7}_{-0.5}$ Gyr (Section 4.2), much older than the model log g values indicate. Using this age, we estimated the log g in Section 5.2.2 to be closer to ∼5.28 dex. Such a large mismatch in estimated surface gravity between this surface gravity and that from the best-fitting model (`Sonora Diamondback`; 3.5 dex) is likely due to incomplete atmospheric chemistry and cloud physics in the model grids.

9.3. Metallicity

BD+24, the host star of CW 2106, has an overall metallicity of [M/H] = 0.00 ± 0.06 dex (Section 4.1.2). As its companion and substellar sibling, CW 2106 should also have the same bulk metallicity. The best-fitting model, `Sonora Diamondback`, has a metallicity of [M/H]=0 dex, in good agreement with the metallicity of BD+24. The best-fitting `Sonora Elf-Owl` model, however, has a supersolar metallicity of 0.5 dex. `Elf-Owl` does not include any contribution of clouds within its model grid, so the supersolar metallicity of the best-fit model may be due to the higher metallicity more closely replicating the reddening effects caused by clouds.

9.4. CW 2106 as a Synthetic Spectrum

Typically, fitting forward model grids to observed spectra is done as a way of inferring the parameters of your object. For

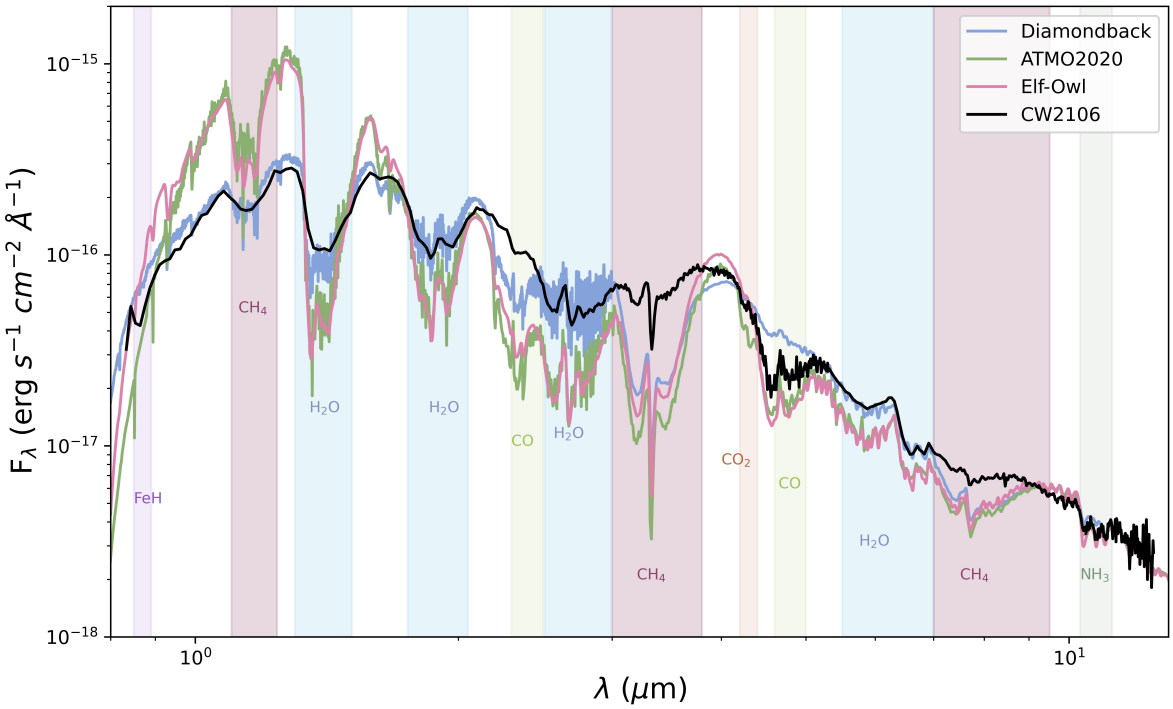


Figure 11. The SED of CW 2106 (in black) along with synthetic SEDs from `Sonora Diamonback` (purple), `Sonora Elf-Owl` (pink), and `ATMO2020` (green). Regions of broad molecular absorptions are highlighted and labeled. All synthetic SEDs were generated for $T_{\rm eff} = 1213$ K, log $g = 5.28$ dex, and [M/H] = 0.00 dex. The `Diamondback` SED was chosen to have $f_{\rm sed} = 6$ for the best visual fit, and both `Elf-Owl` and `ATMO2020` SEDs have log(K_{zz})=3 dex.

isolated field brown dwarfs, there are not many ways in which one can determine the plausibility of these parameters, leading one to rely on the ability of the models to accurately produce the spectra for a variety of different objects. In the case of CW 2106, as discussed above, the parameters of the best-fit models in Section 7.2.1 do not match what we would expect from the analysis of its host star, which, if it were isolated, could possibly lead to an incorrect conclusion as to the nature of CW 2106.

While the model parameters provide a poor fit to those of CW 2106, we can also ask another important question: how well do the models reproduce the SED of CW 2106 using its *actual* fundamental parameters? To answer this, we used `SEDA` to generate synthetic SEDs for each of the three models used in Section 7, interpolating between model grid points to obtain models with the exact $T_{\rm eff}$, log g, and [M/H] of CW 2106 (Section 5.2.2) and solar C/O (as all but the `Elf-Owl` models only consider solar C/O). For `Sonora Diamondback`, we did this for $f_{\rm sed}$ values of 2, 4, 6, and 8, settling with a final value of $f_{\rm sed} = 6$ due to its best visual fit. Likewise, the log K_{zz} for both the `Elf-Owl` and `ATMO2020` were chosen via best visual fit as log $K_{zz} = 3$ dex.

The final synthetic SEDs are shown along with the observed SED of CW 2106 in Figure 11. Visually, `Diamondback` provides the best fit to the SED of CW 2106 of all three synthetic SEDs used, although there are many regions where the models all fail to replicate the spectral features of CW 2106. With the best-fitting SED, from `Sonora Diamondback`, the model overpredicts the flux in the *Y* and *J* bands. Likewise, `Diamondback` also overpredicts the amount of flux around ∼1.6 μm at the start of the *H*-band. Overall, `Diamondback` is able to replicate the depth of H_2O bands throughout the near-IR. However, at 2.2 μm, `Diamondback` has much stronger CH_4 absorption than is seen in CW 2106. This is also true of the 3.3 μm CH_4 feature, which in the synthetic `Diamondback` SED is significantly deeper than that of CW 2106. The 4 μm peak of the `Diamondback` SED is much sharper than that of CW 2106, lacks the 4.2 μm CO_2 absorption feature, and is underluminous. The 4.6 μm CO feature, while present in the `Diamondback` SED, is considerably shallower than is actually observed, leading to an excess of flux in that region. In the mid-IR, while the depth of the H_2O in `Diamondback` is comparable to CW 2106, the CH_4 is once again overpredicted, with a much stronger 7–9 μm feature in the `Diamondback` SED. The 10.5 μm NH_3 feature observed in CW 2106 is also reproduced by the `Diamondback` model.

The `Elf-Owl` and `ATMO2020` synthetic SEDs perform similarly to the `Diamondback` model, with stronger CH_4 features and overluminous *J* and *H* bands. However, these SEDs also have much deeper H_2O across the full wavelength range, likely because both the `Elf-Owl` and `ATMO2020` lack clouds, which have been shown to weaken these features (C. V. Morley et al. 2024). Unlike the SED generated with the `Diamondback` models, the `Elf-Owl` and `ATMO2020` SEDs are able to accurately reproduced the observed 4.6 μm CO band depth, possibly due to the addition of disequilibrium chemistry within these models, unlike with the `Diamondback` models. The 4.2 μm CO_2 absorption feature in the `Elf-Owl` is weaker than observed in CW 2106, while the CO_2 in `ATMO2020` appears to be stronger than is observed. Previous studies have also found an underprediction of CO_2 using the `Elf-Owl` models.

10. Conclusions

In this paper, we present the 0.8–12.5 μm SED, obtained with JWST and Magellan/FIRE, for the T0 ± 1 dwarf CWISE J210640.16+250729.0, a companion to the K6V dwarf BD+24 4329. Using high resolution ($R \sim 60{,}000$)

spectroscopy of the host star, we derive elemental abundances for the system, finding it to be solar ([M/H] = 0.00 dex) with an average Mg/Si ratio (Mg/Si = 0.87). We derive a system age of $3.3^{+0.7}_{-0.5}$ Gyr using model isochrones and gyrochronolgy, and fit its galactic orbit using Gaia DR3 kinematics, placing it within the thin disk population.

We semiempirically derived the mass (M), radius (R), surface gravity ($\log g$), effective temperature ($T_{\rm eff}$), and bolometric luminosity for CW 2106 using its full SED along with the age and distance adopted from its host star, finding values of 50–62 $M_{\rm Jup}$, 0.83–0.87 $R_{\rm Jup}$, 5.21–5.35 dex, 1213 ± 21 K, and −4.825 ± 0.005 dex, respectively. Comparing these with literature values for other brown dwarfs, we find CW 2106 is normal for its spectral type in $T_{\rm eff}$, but underluminous compared with other objects of a similar temperature. We then presented an analysis of the spectral features observed in the JWST spectra, visually inspecting and calculating spectral indices of H_2O, CH_4, NH_3, and silicate condensates, placing these measurements into context with the broader field population, highlighting the ability of JWST to drastically reduce the errors associated with these calculations.

We fit a series of different atmospheric model grids to the SED of CW 2106 and find that the best-fitting models require the inclusion of clouds, despite the lack of a silicate feature in the MIRI LRS spectrum. Fitting only portions of the SED provides inconsistent best-fit model parameters depending on the region of choice. Thanks to the benchmark nature of CW 2106, we are able to test the ability of current atmospheric models to accurately reproduce observed data. We find that all models prefer hotter $T_{\rm eff}$ values and lower $\log g$ than was independently derived for CW 2106, while models generated using the actual parameters of CW 2106 fail to match its spectral morphology.

While the atmospheric models are poor fits to the data, the preference for cloudy models, particularly in the near-IR (which probes the deepest atmospheric pressures), and the red color of CW 2106, leads us to conclude that deep clouds in its atmosphere are likely helping to shape the SED of CW 2106. This modeling suggests a cloudy near-IR photosphere, but a cloudless mid-IR photosphere. Using updated thermochemical models, as well as the Mg/Si ratio of the host star, we find that these clouds are expected to be comprised of $MgSiO_3$. Future atmospheric retrievals may be able to identify and confirm the species present (e.g., B. Burningham et al. 2021; J. M. Vos et al. 2023).

This study highlights the immense power of using JWST's high signal, broad wavelength coverage observations with benchmark brown dwarfs. These JWST benchmarks will serve as a "Rosetta Stone," helping to decode and understand the roles that age, composition, and gravity play in sculpting substellar spectra.

Acknowledgments

We thank Johanna Teske for helpful conversations that improved the paper. This paper includes data taken at The McDonald Observatory of The University of Texas at Austin. This paper includes data gathered with the 6.5 m Magellan Telescopes located at Las Campanas Observatory, Chile. B.B. acknowledges support from UK Research and Innovation Science and Technology Facilities Council [ST/X001091/1]. V.K. acknowledges support from a UK Science and Technology Facilities Council studentship. J.F. and A.R. acknowledge support from NASA award 80NSSC22K0491, STSCI award JWST-GO-03670.002-A, and NSF award 2238468. J.M.V acknowledges funding from European Research Council Starting Grant Exo-PEA (grant agreement No. [101164652]). This work presents results from the European Space Agency (ESA) space mission Gaia. Gaia data are being processed by the Gaia Data Processing and Analysis Consortium (DPAC). Funding for the DPAC is provided by national institutions, in particular the institutions participating in the Gaia MultiLateral Agreement (MLA). The Gaia mission website is https://www.cosmos.esa.int/gaia. The Gaia archive website is https://archives.esac.esa.int/gaia. This publication makes use of data products from the Wide-field Infrared Survey Explorer, which is a joint project of the University of California, Los Angeles, and the Jet Propulsion Laboratory/California Institute of Technology, funded by the National Aeronautics and Space Administration.

Facilities: JWST, Smith, Magellan:Baade.

Software: Sedkit (J. Filippazzo 2020), JWST Science Calibration Pipeline (H. Bushouse et al. 2022), `BACCHUS` (T. Masseron et al. 2016), `galpy` (J. Bovy 2015), `stardate` (R. Angus et al. 2019), `SEDA` (G. Suárez et al. 2021, Suarez et al. 2026, in preparation), astropy, matplotlib.

Appendix A
Differential Brewer Star Comparison

HD 131582 and HD 144872 were observed as part of the J. M. Brewer et al. (2016) planet-search stars spectral catalog (hereinafter the Brewer catalog). All stars were observed with the HIRES spectrograph ($R \sim 70{,}000$) located on the Keck I telescope over a variety of different radial velocity based planet searches. The spectra were uniformly analyzed using a procedure based on the Spectroscopy Made Easy (SME; J. A. Valenti & N. Piskunov 1996) package, obtaining precise fundamental parameters (e.g., $T_{\rm eff}$, $\log g$, $v\sin(i)$, etc.) and abundances for 15 elements using the Vienna Atomic Line Database (VALD-3).

HD 131582 and HD 144872 were used as standards in our differential abundance analysis of BD+24 (Section 4.1.1), using their parameters from J. M. Brewer et al. (2016) along with their observed spectra (3.3) to calculate BD+24's offsets in each parameter from both standards. However, we also used this methodology to get the differential abundances of HD 131582 with respect to HD 144872, and vice versa. Comparing the results we get from this analysis with the ground truth values from J. M. Brewer et al. (2016) provides a way of testing the performance of this analysis.

The parameters of HD 131582 and HD 144872 from both `BACCHUS` and J. M. Brewer et al. (2016) are listed in Table A1. Overall, our results using `BACCHUS` are in good agreement with those of the Brewer catalog. The `BACCHUS` $T_{\rm eff}$'s for HD 131582 and HD 144872 are consistent within $\lesssim 1.7\sigma$ of those derived in J. M. Brewer et al. (2016). Likewise, the `BACCHUS` values for $\log g$ and [M/H] are consistent within $\lesssim 1\sigma$ and $\lesssim 1.2\sigma$, respectively.

Comparing the individual elemental abundances (Figure A1) between our work and that of J. M. Brewer et al. (2016) shows that the majority of elements for both HD 131582 and HD 144872 are consistent within $\lesssim 2\sigma$. There are some noticeable departures, however. With HD 131582, for example, the [O/H] values derived by J. M. Brewer et al. (2016) and those derived in

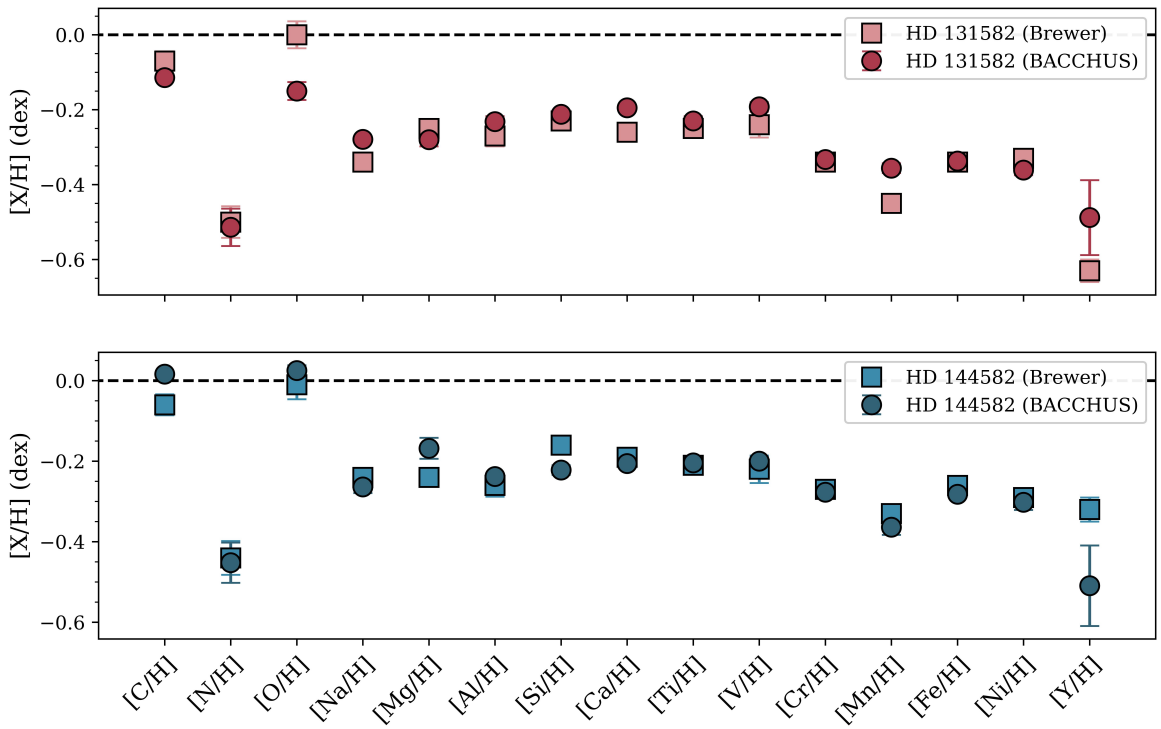


Figure A1. Top: elemental abundances for HD 131582 from BACCHUS (circles) and from J. M. Brewer et al. (2016; squares) and their associated errors. The dashed line represents the reference solar value of 0. Bottom: same as in the top panel, but for HD 144872.

Table A1
Differential Abundance Comparison

Property	HD 131582		HD 144872	
	Lit.[a]	BACCHUS[b]	Lit.[a]	BACCHUS[c]
$T_{\rm eff}$ (K)	4728 ± 25	4772 ± 8	4780 ± 25	4814 ± 32
log g (dex)	4.52 ± 0.03	4.58 ± 0.54	4.52 ± 0.03	4.58 ± 0.40
[M/H] (dex)	−0.29 ± 0.01	−0.31 ± 0.08	−0.26 ± 0.01	−0.20 ± 0.05
[Fe/H] (dex)	−0.34 ± 0.01	−0.34 ± 0.01	−0.26 ± 0.01	−0.28 ± 0.01
[C/H] (dex)	−0.07 ± 0.03	−0.11 ± 0.01	−0.06 ± 0.03	0.02 ± 0.01
[N/H] (dex)	−0.50 ± 0.03	−0.51 ± 0.05	−0.44 ± 0.03	−0.45 ± 0.05
[O/H] (dex)	0.00 ± 0.04	−0.15 ± 0.02	−0.01 ± 0.04	0.03 ± 0.01
[Mg/H] (dex)	−0.25 ± 0.01	−0.28 ± 0.02	−0.24 ± 0.01	−0.17 ± 0.03
[Si/H] (dex)	−0.23 ± 0.01	−0.21 ± 0.01	−0.16 ± 0.01	−0.22 ± 0.01
[Ca/H] (dex)	−0.26 ± 0.01	−0.20 ± 0.01	−0.19 ± 0.01	−0.21 ± 0.01
[Na/H] (dex)	−0.34 ± 0.01	−0.28 ± 0.01	−0.24 ± 0.01	−0.26 ± 0.02
[Al/H] (dex)	−0.27 ± 0.03	−0.23 ± 0.02	−0.26 ± 0.03	−0.24 ± 0.01
[Ti/H] (dex)	−0.25 ± 0.01	−0.23 ± 0.01	−0.21 ± 0.01	−0.20 ± 0.01
[V/H] (dex)	−0.24 ± 0.03	−0.19 ± 0.01	−0.22 ± 0.03	−0.20 ± 0.01
[Cr/H] (dex)	−0.34 ± 0.01	−0.33 ± 0.01	−0.27 ± 0.01	−0.28 ± 0.01
[Mn/H] (dex)	−0.45 ± 0.02	−0.36 ± 0.01	−0.33 ± 0.02	−0.36 ± 0.02
[Ni/H] (dex)	−0.33 ± 0.01	−0.36 ± 0.01	−0.29 ± 0.01	−0.30 ± 0.02
[Y/H] (dex)	−0.63 ± 0.03	−0.49 ± 0.10	−0.32 ± 0.03	−0.51 ± 0.10
C/O	0.47 ± 0.04[d]	0.60 ± 0.02	0.49 ± 0.04[d]	0.54 ± 0.01
Mg/Si	0.98 ± 0.01[d]	0.87 ± 0.02	0.85 ± 0.01[d]	1.15 ± 0.03

Notes.
[a] Literature values from J. M. Brewer et al. (2016).
[b] BACCHUS derived differential abundances with respect to HD 144872.
[c] BACCHUS derived differential abundances with respect to HD 131582.
[d] This value was derived in this study from the abundances presented in J. M. Brewer et al. (2016).

this study differ by ∼3.4σ, with $[O/H]_{\rm Brewer} = 0.00 \pm 0.04$ and $[O/H]_{\rm BACCHUS} = -0.15 \pm 0.02$. [Mn/H] is also slightly different. The results for [Ca/H] and [Na/H] in HD 133582 are each discrepant by ∼6σ. This difference, however, seems to be driven by the very small uncertainties in our BACCHUS values (<0.01 dex), rather than substantial differences between the two results.

Due to the slight differences in individual elemental abundances, the C/O and Mg/Si ratios of HD 131582 are a bit discrepant, with differences of 2.9σ and 4.9σ, respectively.

The BACCHUS individual abundances of HD 144872 have an overall stronger agreement with J. M. Brewer et al. (2016) than was seen in HD 131582. However, one major difference is between the measured [Si/H], which differ by $\sim 4.2\sigma$. While both J. M. Brewer et al. (2016) and our study find subsolar values of [Si/H] for HD 144872, our results show a slightly more subsolar value. As a result, the Mg/Si values for HD 144872 differ substantially ($\sim 9.5\sigma$).

One important caveat is that these differential abundances for HD 131582 and HD 144872 were derived using only one reference star from which their differences were calculated. Ideally, these differences would be calculated with multiple reference stars as was done in Section 4.1.1 for BD+24. Future works will expand on these differential abundances using more sources from J. M. Brewer et al. (2016), allowing for a proper benchmarking of the technique.

Appendix B
Raw Differential Abundances for BD+24

As discussed in Section 4.1.1, the abundances for BD+24 presented in Appendix A are derived by comparing the spectra, line by line, between BD+24 and the reference stars HD 131582 and HD 144872, determining the difference in absolute abundance between each star. These differences are then applied to the final abundance results presented in J. M. Brewer et al. (2016) to get the corresponding "absolute" abundances for BD+24. However, this method limits the analysis to the 15 elements investigated by J. M. Brewer et al. (2016), as these are the only values to which we can apply BD +24's offsets. Using BACCHUS with the broadband wavelength coverage spectra obtained with the Tull Coude Spectrograph (Section 3.3), our analysis is sensitive to 26 individual elements. Table B1 presents the raw differential abundances (i.e., Δ[X/H]) for BD+24 with respect to both HD 131582 and HD 144872 for all elements we are able to constrain using BACCHUS.

Table B1
BD+24 Raw Differential Abundances

Property	Δ_{131}[a]	Δ_{144}[b]
$\Delta T_{\rm eff}$ (K)	−228.00 ± 79.00	−268.00 ± 21.00
$\Delta \log g$ (dex)	−0.13 ± 0.05	−0.02 ± 0.10
Δ[M/H] (dex)	0.29 ± 0.26	0.26 ± 0.06
Δv_{mic} (Km s^{-2})	0.00 ± 0.13	0.00 ± 0.03
Δ[C/H] (dex)	0.24 ± 0.02	0.22 ± 0.02
Δ[N/H] (dex)	0.25 ± 0.05	0.25 ± 0.05
Δ[O/H] (dex)	0.11 ± 0.08	0.10 ± 0.09
Δ[Na/H] (dex)	0.20 ± 0.10	⋯
Δ[Mg/H] (dex)	0.36 ± 0.03	0.32 ± 0.01
Δ[Al/H] (dex)	0.24 ± 0.01	0.17 ± 0.01
Δ[Si/H] (dex)	0.35 ± 0.07	0.35 ± 0.06
Δ[Ca/H] (dex)	0.29 ± 0.03	0.19 ± 0.03
Δ[Sc/H] (dex)	0.34 ± 0.04	0.22 ± 0.04
Δ[Cr/H] (dex)	0.26 ± 0.01	0.18 ± 0.01
Δ[Ti/H] (dex)	0.18 ± 0.04	0.16 ± 0.02
Δ[V/H] (dex)	0.22 ± 0.10	0.15 ± 0.01
Δ[Mn/H] (dex)	0.36 ± 0.10	0.21 ± 0.10
Δ[Co/H] (dex)	0.23 ± 0.05	0.32 ± 0.04
Δ[Fe/H] (dex)	0.30 ± 0.01	0.25 ± 0.01
Δ[Ni/H] (dex)	0.31 ± 0.02	0.27 ± 0.02
Δ[Cu/H] (dex)	0.26 ± 0.10	0.26 ± 0.10
Δ[Zn/H] (dex)	0.17 ± 0.02	0.16 ± 0.02
Δ[Y/H] (dex)	⋯	0.29 ± 0.10
Δ[Zr/H] (dex)	0.40 ± 0.02	0.19 ± 0.03
Δ[Mo/H] (dex)	0.31 ± 0.01	0.23 ± 0.10
Δ[Ba/H] (dex)	0.30 ± 0.10	0.02 ± 0.10
Δ[La/H] (dex)	0.40 ± 0.05	⋯
Δ[Nd/H] (dex)	0.26 ± 0.10	⋯

Notes.
[a] Differential values with respect to HD 131582.
[b] Differential values with respect to HD 144872.

ORCID iDs

Austin Rothermich https://orcid.org/0000-0003-4083-9962
Jacqueline K. Faherty https://orcid.org/0000-0001-6251-0573
Ben Burningham https://orcid.org/0000-0003-4600-5627
Catherine Manea https://orcid.org/0000-0002-0900-6076

Emily Calamari https://orcid.org/0000-0002-2682-0790
Genaro Suárez https://orcid.org/0000-0002-2011-4924
Daniella C. Bardalez Gagliuffi https://orcid.org/0000-0001-8170-7072
John M. Brewer https://orcid.org/0000-0002-9873-1471
Kelle L. Cruz https://orcid.org/0000-0002-1821-0650
Jonathan Gagné https://orcid.org/0000-0002-2592-9612
Eileen C. Gonzales https://orcid.org/0000-0003-4636-6676
Marina E. Gemma https://orcid.org/0000-0002-8871-773X
Viktória Kecskeméthy https://orcid.org/0000-0002-9511-0901
Mark S. Marley https://orcid.org/0000-0002-5251-2943
Caprice L. Phillips https://orcid.org/0000-0001-5610-5328
Channon Visscher https://orcid.org/0000-0001-6627-6067
Johanna M. Vos https://orcid.org/0000-0003-0489-1528
Niall Whiteford https://orcid.org/0000-0001-8818-1544

References

Ackerman, A. S., & Marley, M. S. 2001, ApJ, 556, 872
Allers, K. N., & Liu, M. C. 2013, ApJ, 772, 79
Anderson, D. R., Collier Cameron, A., Hellier, C., et al. 2011, ApJL, 726, L19
Angus, R., Morton, T. D., Foreman-Mackey, D., et al. 2019, AJ, 158, 173
Bardalez Gagliuffi, D. C., Burgasser, A. J., Schmidt, S. J., et al. 2019, ApJ, 883, 205
Bate, M. R. 2009, MNRAS, 392, 590
Bate, M. R. 2012, MNRAS, 419, 3115
Bate, M. R., Bonnell, I. A., & Bromm, V. 2002, MNRAS, 332, L65
Bedell, M., Bean, J. L., Meléndez, J., et al. 2018, ApJ, 865, 68
Beiler, S. A., Cushing, M. C., Kirkpatrick, J. D., et al. 2023, ApJL, 951, L48
Beiler, S. A., Cushing, M. C., Kirkpatrick, J. D., et al. 2024, ApJ, 973, 107
Best, W. M. J., Liu, M. C., Magnier, E. A., & Dupuy, T. J. 2020, AJ, 159, 257
Best, W. M. J., Sanghi, A., Liu, M. C., Magnier, E. A., & Dupuy, T. J. 2024, ApJ, 967, 115
Blanco-Cuaresma, S., Soubiran, C., Heiter, U., & Jofré, P. 2014, A&A, 569, A111
Bland-Hawthorn, J., & Gerhard, O. 2016, ARA&A, 54, 529
Bochanski, J. J., Hennawi, J. F., Simcoe, R. A., et al. 2009, PASP, 121, 1409
Bovy, J. 2015, ApJS, 216, 29
Brewer, J. M., & Fischer, D. A. 2016, ApJ, 831, 20
Brewer, J. M., Fischer, D. A., Valenti, J. A., & Piskunov, N. 2016, ApJS, 225, 32
Burgasser, A. J., Geballe, T. R., Leggett, S. K., Kirkpatrick, J. D., & Golimowski, D. A. 2006, ApJ, 637, 1067
Burgasser, A. J., Kirkpatrick, J. D., Brown, M. E., et al. 2002b, ApJ, 564, 421
Burgasser, A. J., Marley, M. S., Ackerman, A. S., et al. 2002a, ApJL, 571, L151
Burningham, B., Marley, M. S., Line, M. R., et al. 2017, MNRAS, 470, 1177
Burningham, B., Faherty, J. K., Gonzales, E. C., et al. 2021, MNRAS, 506, 1944
Burrows, A., Marley, M., Hubbard, W. B., et al. 1997, ApJ, 491, 856
Burrows, A., & Sharp, C. M. 1999, ApJ, 512, 843
Bushouse, H., Eisenhamer, J., Dencheva, N., et al. 2022, JWST Calibration Pipeline v1.8.2, Zenodo, doi:10.5281/zenodo.7229890
Calamari, E., Faherty, J. K., Visscher, C., et al. 2024, ApJ, 963, 67
Calamari, E., Faherty, J. K., Burningham, B., et al. 2022, ApJ, 940, 164
Carmichael, T. W. 2023, MNRAS, 519, 5177
Carmichael, T. W., Latham, D. W., & Vanderburg, A. M. 2019, AJ, 158, 38
Carmichael, T. W., Quinn, S. N., Mustill, A. J., et al. 2020, AJ, 160, 53
Carmichael, T. W., Quinn, S. N., Zhou, G., et al. 2021, AJ, 161, 97
Chabrier, G., Baraffe, I., Allard, F., & Hauschildt, P. 2000, ApJ, 542, 464
Chabrier, G., Baraffe, I., Phillips, M., & Debras, F. 2023, A&A, 671, A119
Chambers, K. C., Magnier, E. A., Metcalfe, N., et al. 2016, arXiv:1612.05560
Choi, J., Dotter, A., Conroy, C., et al. 2016, ApJ, 823, 102
Cushing, M. C., Kirkpatrick, J. D., Gelino, C. R., et al. 2011, ApJ, 743, 50
Cushing, M. C., Marley, M. S., Saumon, D., et al. 2008, ApJ, 678, 1372
Cushing, M. C., Roellig, T. L., Marley, M. S., et al. 2006, ApJ, 648, 614
Cushing, M. C., Vacca, W. D., & Rayner, J. T. 2004, PASP, 116, 362
Cutri, R. M., Wright, E. L., Conrow, T., et al. 2021, yCat, II/328. Originally published in: IPAC/Caltech (2013)
Díaz, R. F., Damiani, C., Deleuil, M., et al. 2013, A&A, 551, L9
Dotter, A. 2016, ApJS, 222, 8
Dupuy, T. J., & Liu, M. C. 2012, ApJS, 201, 19
Dupuy, T. J., & Liu, M. C. 2017, ApJS, 231, 15
Dye, S., Lawrence, A., Read, M. A., et al. 2018, MNRAS, 473, 5113
Eriksson, S. C., Janson, M., & Calissendorff, P. 2019, A&A, 629, A145
Faherty, J. K., Burgasser, A. J., Walter, F. M., et al. 2012, ApJ, 752, 56
Faherty, J. K., Riedel, A. R., Cruz, K. L., et al. 2016, ApJS, 225, 10
Filippazzo, J. 2020, SEDkit: Spectral energy distribution construction and analysis tools, Astrophysics Source Code Library, ascl:2011.014
Filippazzo, J., Alejandro Merchan, S., & Cruz, K. 2025, sedkit, v2.1, Zenodo, doi:10.5281/zenodo.15013812
Filippazzo, J. C., Rice, E. L., Faherty, J., et al. 2015, ApJ, 810, 158
Fontaine, G., Brassard, P., & Bergeron, P. 2001, PASP, 113, 409
Gaarn, J., Burningham, B., Faherty, J. K., et al. 2023, MNRAS, 521, 5761
Gagné, J., Faherty, J. K., Cruz, K. L., et al. 2015, ApJS, 219, 33
Gagné, J., Faherty, J. K., Schneider, A. C., & Meisner, A. M. 2021, CoMover: Bayesian probability of co-moving stars, Astrophysics Source Code Library, ascl: 2106.007
Gagné, J., Lafrenière, D., Doyon, R., Malo, L., & Artigau, É. 2014, ApJ, 783, 121
Gagné, J., Mamajek, E. E., Malo, L., et al. 2018, ApJ, 856, 23
Gaia Collaboration, Prusti, T., de Bruijne, J., H., J., et al. 2016, A&A, 595, A1
Gaia Collaboration, Smart, R. L., Sarro, L. M., et al. 2021, A&A, 649, A6
Gaia Collaboration, Vallenari, A., Brown, A. G. A., et al. 2023, A&A, 674, A1
Gonzales, E. C., Burningham, B., Faherty, J. K., et al. 2020, ApJ, 905, 46
Gustafsson, B., Edvardsson, B., Eriksson, K., et al. 2008, A&A, 486, 951
Hawkins, K., Lucey, M., Ting, Y.-S., et al. 2020, MNRAS, 492, 1164
Hayes, C. R., Masseron, T., Sobeck, J., et al. 2022, ApJS, 262, 34
Heiter, U., Lind, K., Bergemann, M., et al. 2021, A&A, 645, A106
Hodžić, V., Triaud, A. H. M. J., Anderson, D. R., et al. 2018, MNRAS, 481, 5091
Hood, C. E., Mukherjee, S., Fortney, J. J., et al. 2024, arXiv:2402.05345
Jakobsen, P., Ferruit, P., Alves de Oliveira, C., et al. 2022, A&A, 661, A80
Jofré, P., Heiter, U., & Soubiran, C. 2019, ARA&A, 57, 571
Johnson, J. A., Apps, K., Gazak, J. Z., et al. 2011, ApJ, 730, 79
Karalidi, T., Marley, M., Fortney, J. J., et al. 2021, ApJ, 923, 269
Kiman, R., Xu, S., Faherty, J. K., et al. 2022, AJ, 164, 62
Kirkpatrick, J. D. 2005, ARA&A, 43, 195
Kirkpatrick, J. D., Cruz, K. L., Barman, T. S., et al. 2008, ApJ, 689, 1295
Kirkpatrick, J. D., Looper, D. L., Burgasser, A. J., et al. 2010, ApJS, 190, 100
Kirkpatrick, J. D., Gelino, C. R., Faherty, J. K., et al. 2021, ApJS, 253, 7
Kirkpatrick, J. D., Marocco, F., Gelino, C. R., et al. 2024, ApJS, 271, 55
Kirkpatrick, J. D., Reid, I. N., Liebert, J., et al. 1999, ApJ, 519, 802
Kirkpatrick, J. D., Reid, I. N., Liebert, J., et al. 2000, AJ, 120, 447
Kothari, H., Cushing, M. C., Burningham, B., et al. 2024, ApJ, 971, 121
Kuchner, M. J., Faherty, J. K., Schneider, A. C., et al. 2017, ApJL, 841, L19
Kurucz, R. L. 1992, IAUS, 149, 225
Lew, B. W. P., Roellig, T., Batalha, N. E., et al. 2024, AJ, 167, 237
Line, M. R., Teske, J., Burningham, B., Fortney, J. J., & Marley, M. S. 2015, ApJ, 807, 183
Liu, F., Asplund, M., Ramirez, I., Yong, D., & Melendez, J. 2014, MNRAS, 442, L51
Liu, M. C., Magnier, E. A., Deacon, N. R., et al. 2013, ApJL, 777, L20
Lodders, K., & Fegley, B., J. 2006, in Astrophysics Update 2, ed. J. W. Mason (Springer), 1
Luhman, K. L. 2007, ApJS, 173, 104
Mamajek, E. E., & Hillenbrand, L. A. 2008, ApJ, 687, 1264
Marley, M. S., Saumon, D., Cushing, M., et al. 2012, ApJ, 754, 135
Marocco, F., Eisenhardt, P. R. M., Fowler, J. W., et al. 2021, ApJS, 253, 8
Masseron, T., Merle, T., & Hawkins, K. 2016, BACCHUS: Brussels Automatic Code for Characterizing High accUracy Spectra, Astrophysics Source Code Library, ascl:1605.004
Masseron, T., Plez, B., Van Eck, S., et al. 2014, A&A, 571, A47
McCarthy, A. M., Muirhead, P. S., Tamburo, P., et al. 2024, ApJ, 965, 83
McGovern, M. R., Kirkpatrick, J. D., McLean, I. S., et al. 2004, ApJ, 600, 1020
McKenzie, M., Yong, D., Marino, A. F., et al. 2022, MNRAS, 516, 3515
Meléndez, J., Bergemann, M., Cohen, J. G., et al. 2012, A&A, 543, A29
Metchev, S. A., & Hillenbrand, L. A. 2006, ApJ, 651, 1166
Morley, C. V., Mukherjee, S., Marley, M. S., et al. 2024, ApJ, 975, 59
Mukherjee, S., Fortney, J. J., Morley, C. V., et al. 2024, ApJ, 963, 73
Nelson, T., Ting, Y.-S., Hawkins, K., et al. 2021, ApJ, 921, 118
Noll, K. S., Geballe, T. R., & Marley, M. S. 1997, ApJL, 489, L87
Nowak, G., Palle, E., Gandolfi, D., et al. 2017, AJ, 153, 131
Oelkers, R. J., Rodriguez, J. E., Stassun, K. G., et al. 2018, AJ, 155, 39
Persson, C. M., Csizmadia, S., Mustill, A. J., et al. 2019, A&A, 628, A64
Phillips, C. L., Faherty, J. K., Burningham, B., et al. 2024, ApJ, 972, 172

Phillips, M. W., Tremblin, P., Baraffe, I., et al. 2020, A&A, 637, A38
Plez, B. 2012, Turbospectrum: Code for spectral synthesis, Astrophysics Source Code Library, ascl: 1205.004
Popinchalk, M., Faherty, J. K., Kiman, R., et al. 2021, ApJ, 916, 77
Radigan, J. 2014, ApJ, 797, 120
Reggiani, H., & Meléndez, J. 2017, CaJPh, 95, 855
Renedo, I., Althaus, L. G., Miller Bertolami, M. M., et al. 2010, ApJ, 717, 183
Rieke, G. H., Wright, G. S., Böker, T., et al. 2015, PASP, 127, 584
Rigby, J., Perrin, M., McElwain, M., et al. 2023, PASP, 135, 048001
Rothermich, A., Faherty, J. K., Bardalez-Gagliuffi, D., et al. 2024, AJ, 167, 253
Sanghi, A., Liu, M. C., Best, W. M. J., et al. 2023, ApJ, 959, 63
Saumon, D., & Marley, M. S. 2008, ApJ, 689, 1327
Saumon, D., Marley, M. S., Cushing, M. C., et al. 2006, ApJ, 647, 552
Simcoe, R. A., Burgasser, A. J., Schechter, P. L., et al. 2013, PASP, 125, 270
Skrutskie, M. F., Cutri, R. M., Stiening, R., et al. 2006, AJ, 131, 1163
Skumanich, A. 1972, ApJ, 171, 565
Sorahana, S., & Yamamura, I. 2012, ApJ, 760, 151
Spina, L., Meléndez, J., Karakas, A. I., et al. 2018, MNRAS, 474, 2580
Stephens, D. C., Leggett, S. K., Cushing, M. C., et al. 2009, ApJ, 702, 154
Stephenson, C. B. 1986, AJ, 91, 144
Suárez, G., & Metchev, S. 2022, MNRAS, 513, 5701
Suárez, G., & Metchev, S. 2023, MNRAS, 523, 4739
Suárez, G., Metchev, S., Leggett, S. K., Saumon, D., & Marley, M. S. 2021, ApJ, 920, 99
Suárez, G., Vos, J. M., Metchev, S., Faherty, J. K., & Cruz, K. 2023, ApJL, 954, L6
Teske, J. K. 2024, ARA&A, 62, 333
Tuchow, N. W., Stark, C. C., & Mamajek, E. 2024, AJ, 167, 139
Turon, C., Creze, M., Egret, D., et al. 1993, BICDS, 43, 5
Vacca, W. D., Cushing, M. C., & Rayner, J. T. 2003, PASP, 115, 389
Valenti, J. A., & Piskunov, N. 1996, A&AS, 118, 595
Visscher, C., Lodders, K., & Fegley, B., Jr. 2010, ApJ, 716, 1060
Vos, J. M., Allers, K. N., & Biller, B. A. 2017, ApJ, 842, 78
Vos, J. M., Burningham, B., Faherty, J. K., et al. 2023, ApJ, 944, 138
Wang, J., Kolecki, J. R., Ruffio, J.-B., et al. 2022, AJ, 163, 189
Werner, M. W., Roellig, T. L., Low, F. J., et al. 2004, ApJS, 154, 1
Wood, M. A. 1995, LNP, 443, 41
Yan, Y., Du, C., Liu, S., et al. 2019, ApJ, 880, 36
Yana Galarza, J., Meléndez, J., Ramírez, I., et al. 2016, A&A, 589, A17
Yong, D., Liu, F., Ting, Y.-S., et al. 2023, MNRAS, 526, 2181
Zalesky, J. A., Saboi, K., Line, M. R., et al. 2022, ApJ, 936, 44